https://doi.org/10.5194/egusphere-2025-6555
Preprint. Discussion started: 30 March 2026


# Looking for Seismic Signatures in the Landscape: A Landslide-Based Record of Holocene Fault Ruptures in the Puget Lowland.

Obinna H Ozioko[1] Adam M. Booth[1] Alison Duvall[2] Erich Herzig[2]

[1] School of Earth, Environment, and Society, Portland State University, Portland, OR 97201, USA

[2] Department of Earth and Space Sciences, University of Washington, Seattle, WA 98195-1310, USA

Correspondence to: ozioko@pdx.edu

## Abstract

Earthquake-triggered landslides pose a major hazard in tectonically active regions and may leave lasting imprints in the landscape that reflect past seismic activity. In the Puget Lowland of Washington State, an urban corridor transected by multiple Holocene-active crustal faults, we investigate whether deep-seated landslides retain a record of prehistoric earthquakes. Using a regional inventory of more than 2,000 deep-seated landslides mapped from high-resolution lidar, we reconstructed a 4,000-year landslide chronology by relating deposit surface roughness to age, calibrated with16 radiocarbon-dated landslides. Temporal clustering of landslides was assessed by identifying peaks in landslide frequency that exceeded a steady-state landslide production model. Those peaks were then compared to earthquake-based scenarios incorporating known ruptures on the Tacoma Fault Zone (TFZ), Seattle Fault Zone (SFZ), Southern Whidbey Island Fault Zone (SWIFZ), and Darrington-Devil's Mountain Fault Zone (DDMFZ). Our reconstructed landslide history reveals clustering of landslides 1000, 1250, 1900, and 2800–3200 years before present (ybp), coinciding with the timing of major Holocene earthquakes around 1000, 2000, and 3000 ybp . A multi-fault earthquake model reproduces these elevated periods more closely than a steady-state scenario. Frequency Ratio (FR) analyses show persistent fault-proximal landslide clustering, particularly along the SFZ and TFZ, where FR decreases with distance from the fault during time intervals containing well-constrained surface rupturing earthquakes. Interpretation of landslide clustering on the DDMFZ is complicated by geomorphic predisposition; on the other hand, weaker signals near SWIFZ likely reflect preservation bias within the landslide record. Nonetheless, temporal and spatial patterns show that Holocene crustal earthquakes generally leave detectable signals in the landslide record of the Puget Lowland. These results show the usefulness of roughness-calibrated landslide chronology as an independent paleoseismic indicator. Overall, this study underscores the value of integrating paleolandslides in reconstructing past earthquake activity and refining hazard assessment in landslide-prone, seismically active landscapes.

https://doi.org/10.5194/egusphere-2025-6555
Preprint. Discussion started: 30 March 2026


## 1.0 Introduction

Landslides are a dangerous secondary effect of earthquakes and can sometimes cause more damage and fatalities than the shaking itself. For example, in the 1920 Haiyuan and 1949 Khait earthquakes, landslides were responsible for about 50% and 98% of all recorded deaths, respectively (Daniell et al., 2017). During the 1987 Ecuador earthquakes, nearly all of the roughly 1,000 fatalities were due to mass wasting (Schuster et al., 1996). Earthquakes with magnitudes of about 7 or higher can trigger thousands of landslides, especially in areas already prone to slope failure (Keefer 1984a). Recent large earthquakes on crustal faults, which often occur at shallow depths and cause strong, localized shaking, have produced many landslides. For example, the May 2008 Wenchuan earthquake in China with Mw 7.9, produced about 200,000 landslides (Xu et al., 2022); the Mw 7.8 November 2016, Kaikoura earthquake in New Zealand triggered around 30,000 landslides (Dellow et al., 2017); and the September 1999 Chi-Chi earthquake in Taiwan (Mw 7.6, about 9,272 landslides; Chang et al., 2005). Most recently, the February 6, 2023, Turkey-Syria earthquake (Mw 7.8) triggered at least 2,800 landslides (Gorum and Tanyas, 2023). Moderate earthquakes have also caused many landslides, such as the September 2018 Hokkaido earthquake in Japan (Mw 6.7, about 6,000 landslides; Kameda et al., 2019) and the January 2009 Cinchona earthquake in Costa Rica (Mw 6.1, about 5,000 landslides; Mendez et al., 2009).

Subduction zone earthquakes, although usually larger, often cause fewer landslides. This is attributed to their deeper source zones and offshore ruptures; shaking intensity is often weaker inland. For example, the 2010 Mw 8.8 earthquake in Chile and the 2011 Mw 9.0 earthquake in Japan produced relatively few landslides for their size (Serey et al., 2019; Wartman et al., 2013). This difference shows that shallow crustal faults, like those in the Puget Lowland, pose a higher landslide risk, especially since these faults run through populated areas. Earthquake-triggered landslides on these faults can threaten lives and property and may also block emergency services from reaching affected areas. In addition to their immediate impact, coseismic landslides can create additional hazards after a large earthquake. Flooding from landslide-dammed lakes and potential breakage of such dams can sustain post-seismic hazards for many years or even decades in mountainous regions (Fan et al., 2019; Yanites et al., 2025). Landslide activity can also persist for weeks, months, or even years after an earthquake, as slopes weakened by shaking fail due to additional triggers (Hovius et al., 2011; Marc et al., 2015; Fan et al., 2019).

https://doi.org/10.5194/egusphere-2025-6555
Preprint. Discussion started: 30 March 2026


Where earthquake-triggered landslides occur depends on the intensity of ground shaking, which usually decreases farther from the fault (Jibson, 1985; Keefer, 2000; Miles & Keefer, 2009). Being close to a fault increases the risk of landslides because shaking is stronger and the ground may shift more (Khazai & Sitar, 2003; Xu et al., 2014). However, landslides do not always follow a simple pattern of decreasing with distance. For example, more landslides occur on the hanging-wall side of reverse or thrust faults due to uneven shaking and the direction of rupture (Meunier et al., 2008; Oglesby et al., 2000). This is also where the land is steeper, which makes landslides more likely even without directivity effects. It can be hard to separate the effects of fault structure from the effects of the landscape, as both can increase landslide risk in these areas. The type of surface material also matters, as evidenced in the Puget Lowland. Previous works have argued that the abundance of weak glacial sediments in the lowland can amplify and prolong seismic shaking, thereby increasing the propensity for slope failure even farther from the fault zone (Herzig et al., 2024; Allstadt et al., 2018; Wartman et al., 2013). Because of these factors, it is important to consider both the tectonic setting and the surface geology when assessing earthquake-related landslide hazards.

Recent progress in studying earthquake-triggered landslides has come from the rapid availability of satellite images after major earthquakes (Wartman et al., 2013; Xu, C., 2015; Tanyas et al., 2022). For example, after the 2013 Lushan earthquake in China, which triggered 3,883 landslides, high-resolution satellite imagery enabled rapid mapping of large landslide areas (Xu et al., 2015). Other cases, such as the Jiuzhaigou earthquake in Sichuan, China, and the 2018 Anchorage earthquake, also showed that satellite images and GIS analysis can help identify landslides quickly, enabling rapid hazard assessment and response (Zheng et al., 2023; Jibson et al., 2020). The use of machine learning in conjunction with remote sensing has enabled faster, more accurate analysis and classification of landslide areas (Tanys et al. 2022). These advances have led to global, standardized datasets of earthquake-triggered landslides, making it easier to compare events worldwide (Tanyas et al., 2017).

Despite advances in modern landslide mapping, we still know little about the patterns and distribution of landslides caused by prehistoric earthquakes, especially in places where earthquakes are rare. This is mainly because it is hard to build a detailed timeline of old landslides. Radiocarbon dating is often used to find the ages of many landslides (Pánek, 2015), but this method

https://doi.org/10.5194/egusphere-2025-6555
Preprint. Discussion started: 30 March 2026


has challenges. The preponderance of landslides in steep, inaccessible areas limit access to dateable materials. Sometimes, the organic material found may be older or younger than the landslide itself, making dating less reliable. As a result, most landslide inventories include only a few well-dated events, limiting our understanding of their timing.

Recently, progress in dating landslides has shown that we can estimate their ages by examining the roughness of their surfaces (Lahusen et al., 2016; Booth et al., 2017; Lahusen et al., 2020; Herzig et al., 2024; Underwood et al., 2025). The idea is that landslide deposits become smoother over time as natural processes erode sharp features and fill in low spots. Younger landslides retain sharper features, such as clear headscarps and uneven surfaces, while older ones blend into the landscape. The availability of high-resolution lidar has paved the way for the accurate quantification of these differences using the wavelet transform or elevation variance that can be matched with radiocarbon ages to create an age-roughness model (Lai et al., 2025; Herzig et al., 2024; LaHusen et al., 2020; Booth et al., 2017). This model helps estimate the ages of landslides that have not been directly dated, enabling the construction of a regional timeline of landslide activity. These timelines can then be used to examine how the timing of ancient earthquakes relates to that of landslides.

This study seeks to construct a regional chronology of landslides in the Puget Lowland by employing lidar-derived surface roughness measurements and age-roughness modeling. The spatio-temporal distribution of landslides is compared with documented Holocene earthquakes across four crustal fault zones to determine whether prehistoric earthquakes left detectable signals in the landslide record. We expect that increased landslide occurrence will coincide with the timing of known fault ruptures. Additionally, we expect spatial clustering of landslides to increase with proximity to the fault, consistent with patterns observed following recent seismic events. Historic earthquakes in the Puget Lowland have been documented to have triggered slope failures. Keefer (1984) noted that the 1949 Mw 7.1 Olympia earthquake and the 1965 Mw 6.5 Seattle-Tacoma earthquakes triggered widespread landsliding in the Puget Lowland. By analyzing the relationship between past earthquakes and landslide patterns, this research aims to improve the understanding of the intensity and spatial extent of ground shaking during unobserved seismic events.

https://doi.org/10.5194/egusphere-2025-6555
Preprint. Discussion started: 30 March 2026


### 1.1 Study Area

Our study area encompasses most of the Puget Lowland (Fig. 1) and was defined based on three main criteria: geologic uniformity, tectonic relevance, and data availability. The eastern boundary was limited to areas underlain by glacial sediments to minimize lithologic variability. The north-south extent was defined to encompass the Seattle, Tacoma, Southern Whidbey Island, and Darrington-Devils Mountain fault zones, allowing assessment of their influence on landslide clustering. The western margin was set by the limit of the available lidar-based landslide inventory (WGS 2020). Although subsets of the study area have been analyzed for spatiotemporal patterns of deep-seated landslides (Booth et al., 2017; Herzig et al., 2024), this study presents the first comprehensive chronology of deep-seated landslide deposits in the region.

The Puget Lowland (Fig. 1) is a north-south trending topographic trough bound by the Olympic Mountains to the west and the Cascade volcanic arc to the east. This low-relief region lies within a forearc basin formed by oblique convergence between the Juan de Fuca and North American plates (Johnson et al., 1999). The landscape of the Puget Lowland has been shaped by repeated episodes of glacial advancement and retreat during the Pleistocene, the most recent being the Puget Lobe during the Vashon Stade of the Fraser Glaciation, which reached its peak at about 14,000 to 15,000 ybp (Porter and Swanson, 1998). In this paper, we will use ybp to refer to calibrated radiocarbon years before present, where “present” is defined as AD 1950. The southward advancement of the Puget Lobe deepened pre-existing valleys and deposited thick sequences of glacial outwash and till. This glacial history resulted in an array of glacial landforms; drumlins, kettle depressions, outwash plains, and proglacial lakes are situated by dominant glacial processes at various parts of the lowland (Booth et al., 2003; Troost and Booth, 2008). The surficial geology of the Puget Lowland reflects a layered history of glacial and interglacial deposits. The Vashon till is the uppermost layer and overlies earlier glacial and non-glacial units, such as the pre-Fraser Lawton Clay, the Olympia beds, and older drift sequences (Troost and Booth, 2008). Beneath the Quaternary sediments, the bedrock geology consists of faulted and folded Tertiary marine and volcanic rocks, including the Eocene Crescent Formation basalts and sedimentary units of the Blakeley and Tukwila formations (Yount et al., 1993). The combination of glacial-carved topography and the distribution of glacial sediments significantly influences slope stability in the Puget Lowland (Tubbs, 1974; Badger, 2015; Perkins et al., 2017). Normally consolidated glacial

https://doi.org/10.5194/egusphere-2025-6555
Preprint. Discussion started: 30 March 2026


sediments – silts, sands, and clays deposited during ice retreat- commonly mantle steep slopes in the Puget Lowland and create the perfect recipe for slope instability. The ubiquitous pattern of permeable, normally consolidated sediments overlying less permeable, overconsolidated layers is a common stratigraphy of the Puget Lowland. Consequently, the buildup of pore pressure from perched groundwater during periods of intense rainfall is a common landslide trigger in the area (Tubbs, 1974; Badger, 2015; Perkins et al., 2017), particularly during the winter months of January and February (Luna and Korup, 2022). However, in addition to groundwater-related landslides, the presence of four Holocene-active crustal fault zones – the Seattle, Tacoma, Southern Whidbey Island, and Darrington–Devils Mountain fault zones, increases the hazard of seismically triggered landslides in the region (Styron and Sherrod, 2021). Paleoseismic investigation has shown that at least one large magnitude earthquake has occurred on each of these fault zones in the last 4000 ybp (Jacoby et al., 1992; Bucknam et al., 1992; Kelsey et al., 2004; Personius et al., 2014; Sherrod, 2001; Sherrod et al., 2008; Nelson et al., 2003, 2008; Black et al., 2024).

The Seattle Fault Zone (SFZ) is well researched, and findings indicate a major earthquake at about 1,100 ybp. Jacoby et al. (1992) provided some of the earliest dendrochronologic evidence of the Seattle Fault earthquake, documenting simultaneously killed and tilted trees in a stand of red cedar near the Seattle waterfront, consistent with an abrupt coseismic deformation. Other studies noted that this event caused up to 7 meters of uplift along Bainbridge Island, generated tsunami deposits, and produced widespread liquefaction features around Puget Sound (Atwater, 1999; Sherrod et al., 2000; Nelson et al., 2003). In a recent study, Black et al. (2024) used tree-ring age dating to constrain this event to the winter of 923–924 CE (1026–1027 ybp), refining previous age estimates. Herzig et al. (2024) also reported increased landslide frequency and spatial patterns in landslide distribution that are coincident with the timing of the most recent Seattle fault rupture.

https://doi.org/10.5194/egusphere-2025-6555
Preprint. Discussion started: 30 March 2026


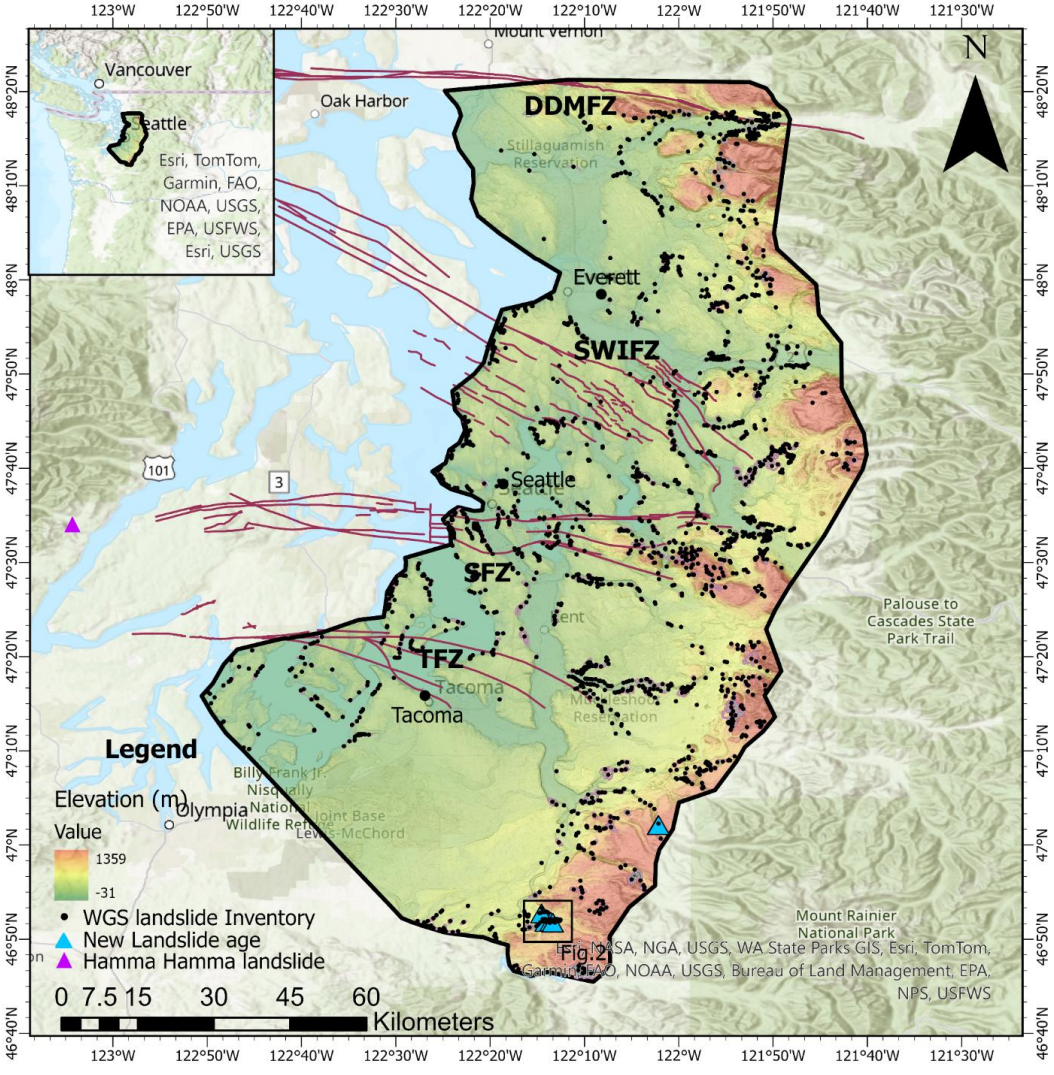


Figure 1 Hillshade map overlain with elevation of the Puget Lowland showing the study area (black outline), the four main crustal faults in red, and the WGS deep-seated landslide inventory (WGS 2020) shown as black dots. DDMFZ = Darrington–Devils Mountain Fault Zone, SWIFZ = South Whidbey Island Fault Zone, SFZ = Seattle Fault Zone, TFZ = Tacoma Fault Zone. Base map: Esri World Hillshade (Esri, USGS, NOAA) | Powered by Esri.

https://doi.org/10.5194/egusphere-2025-6555
Preprint. Discussion started: 30 March 2026


The **Tacoma Fault Zone** (TFZ), located about 25 km south of the SFZ, also shows geomorphic evidence of Holocene activity. While less precisely dated, the most recent event on the TFZ ranges from 930 to 1290 ybp (Bucknam et al., 1992; Sherrod, 2001; Nelson et al., 2008), overlapping the timing of the 1026–1027 ybp SFZ rupture. This has led to suggestions that earthquakes on the two faults could have been synchronous or closely spaced (Blakely et al., 2002; Sherrod et al., 2004). Structural analyses by Blakely et al (2002) reveal that the SFZ and TFZ are part of a crustal-scale duplex system underlying the Seattle Uplift, a geometry that could permit stress transfer and linked rupture. Sherrod et al. (2004) noted that the TFZ earthquake may represent an independent event of similar age or a synchronous rupture with the SFZ, although this linkage is based on timing overlap rather than physical evidence.

Paleoseismic studies on the Southern Whidbey Island Fault Zone (SWIFZ) have documented four measurable surface-rupturing earthquakes during the Holocene, the most recent of which occurred around 2,800–3,200 ybp (Kelsey et al., 2004). Further investigation and offset measurement show that the SWIFZ can produce Mw 6.5–7.0 earthquakes (Sherrod et al., 2008).

Similar paleoseismic trenching studies on the Darrington–Devils Mountain Fault Zone (DDMFZ) at Lake Creek provide evidence for at least one Holocene surface-rupturing earthquake and possibly a second, earlier event (Personius et al., 2014). Evidence from trenching and coring at Lake Creek has constrained the timing of this event to 2300-1500 ybp, with OxCal modeling yielding clustered estimates of 2200 ± 100 ybp and 1900 ± 400 ybp (Personius et al., 2014). For our modelling purposes, we adopt 2000 ybp, an age near the midpoint of this range, to represent the timing of this earthquake on the DDMFZ.

Another potential crustal source at the southern end of the Puget Lowland is the Olympia fault zone (or Olympia lineament), a northwest-trending structure expressed in aeromagnetic and lidar data (Blakely et al., 2002; Walsh et al., 2003). Unlike the other major crustal faults, the Olympia fault lacks detailed paleoseismic trenching studies, and its Holocene activity remains uncertain. Although its seismic potential is therefore ambiguous, its location at the southern boundary of our study area suggests it may also contribute to crustal seismic hazard in the region. The Saddle Mountain Fault, though located at the eastern base of the Olympic Mountains, is another crustal

https://doi.org/10.5194/egusphere-2025-6555
Preprint. Discussion started: 30 March 2026


seismic source linked to a synchronous rupture with the Seattle Fault (Black et al., 2024) during the winter of 923–924 CE (1026–1027 ybp) event.

Paleoseismic evidence indicates that the TFZ, SFZ, SWIFZ, and DDMFZ account for most of the crustal seismic sources in the Puget Lowland that have produced high-magnitude earthquakes. Recent studies by Herzig et al. (2024) and Underwood et al. (2025) have clearly demonstrated that landslides triggered by past earthquakes may leave a detectable signature in the geomorphic record.

## 2.0 Methodology

### 2.1 Landslide Mapping

Using 1-m resolution slope and hillshade derivatives of bare-earth lidar digital elevation models (DEMs), the Washington Geological Survey (WGS) conducted deep-seated landslide mapping across the Puget Lowland, following its standardized protocol (WGS, 2020; Slaughter et al., 2017). The WGS protocol focuses on the use of key geomorphic signatures such as arcuate headscarps, hummocky or disrupted topography, and downslope translation or flow-like deposit to manually delineate landslides while also distinguishing among landslide types, estimating failure depth, volume, and noting secondary features like internal scarps.

Guided by initial landslide mapping outlines, we carried out limited refinements to the WGS statewide landslide inventory (WGS, 2020), incorporating detailed landslide data from previous county-level mapping efforts across the region. This included 10,285 landslides from inventories for western King County (Mickelson et al., 2019), Pierce County (Mickelson et al., 2017), and portions of Snohomish County (Mickelson et al., 2022). Landslide mapping was restricted to deep-seated landslides, defined in the protocol (WGS, 2020; Slaughter et al., 2017) as landslides with failure planes below the depth of tree roots, typically greater than 3 m. The presence of distinctive topographic features, such as hummocky topography downslope of arcuate scarps, over-steepened toes, transverse ridges, and lateral margins, aided the demarcation of deep-seated landslides from other topographic features (Haugerud, 2014; Badger, 2015). The mapped landslides included translational and rotational slides, earthflows, and complex movement types. Using the WGS mapping protocol (WGS, 2020) enabled the semi-automated calculation and recording of landslide

https://doi.org/10.5194/egusphere-2025-6555
Preprint. Discussion started: 30 March 2026


area and volume, the minimum failure depth inferred from scarp height, and the azimuth. Internal features such as scarps, transverse and radial cracks, gullies, and reactivated toes were also mapped and annotated. These features aided field targeting for radiocarbon sampling in this study.

### 2.2 Radiocarbon Sampling and Dating

Fieldwork for a constrained subset of landslides was carried out to validate the remote mapping and to obtain radiocarbon samples for landslide age dating (Fig. 2). We validated mapped landslides based on direct observation and matching of mapped landslide boundaries to features including intact or degraded headscarps, hummocky topography, internal scarps, and signs of reactivation. Ground-truthing confirmed the presence of individual landslide deposits and their relative morphologic freshness, guiding decisions about where to target radiocarbon sampling. Sites with clear evidence of toe erosion or fluvial incision were prioritized for sampling, as these locations often exposed buried organic material suitable for radiocarbon dating.

The landscape is rife with abundant vegetation, some of which has long residence times, up to thousands of years. The abundant vegetative cover increases the likelihood that datable materials will be incorporated into the landslide deposit, thereby making radiocarbon dating ideal for the study area. However, the abundance of organic material in the study area also introduces some uncertainty in the use of radiocarbon for age dating (Pánek, 2015). With long residence times, older organic materials, such as charcoal, can be incorporated into the landslide deposit. Landslide reactivation and animal burrowing can incorporate younger and older organic materials into the landslide body, thereby introducing uncertainty into sampling and the ages obtained. To combat this, sampling was focused on pre-identified geomorphic features likely to re-expose organic material, such as eroded landslide toes along the outer bends of a drainage meander and incised gullies within the landslide body. During sampling, preference was given to large woody logs embedded in stratigraphically secure positions (Fig. 2), with their long axes oriented in the general direction of motion of the landslide body. For each landslide, a minimum of 2 buried wood samples were carefully collected, one near the failure plane and the other higher up in the landslide deposit. Only samples with minimal potential for reworking, clear stratigraphic context, and intact structure were retained for age-roughness model development. This was done to enhance the robustness of our sampling and to help minimize uncertainties in the obtained age. Samples were collected using

https://doi.org/10.5194/egusphere-2025-6555
Preprint. Discussion started: 30 March 2026


a penknife; speck-sized pieces of the logs were collected from the outermost growth rings and preserved in a pocket-sized aluminum bag. Samples were rinsed with deionized water, dried for 24 hrs in an oven, and then sent to the National Ocean Sciences Accelerator Mass Spectrometry facility (NOSAMS) for laboratory analysis and age dating. Using the OxCal 4.4 platform (Bronk Ramsey, 2009) and the IntCal20 curve (Reimer et al. 2020), the radiocarbon ages were calibrated to calendar years before present (ybp). Calibrated age distributions often exhibit complex shapes, with multiple probability peaks and gaps. This is more prevalent in younger samples that fall within calibration curve plateaus. In this study, we assign ages based on the maximum probability density. This method identifies the most likely landslide timing within the 95% confidence interval and avoids biases that can arise from averaging across multiple age modes.

https://doi.org/10.5194/egusphere-2025-6555
Preprint. Discussion started: 30 March 2026


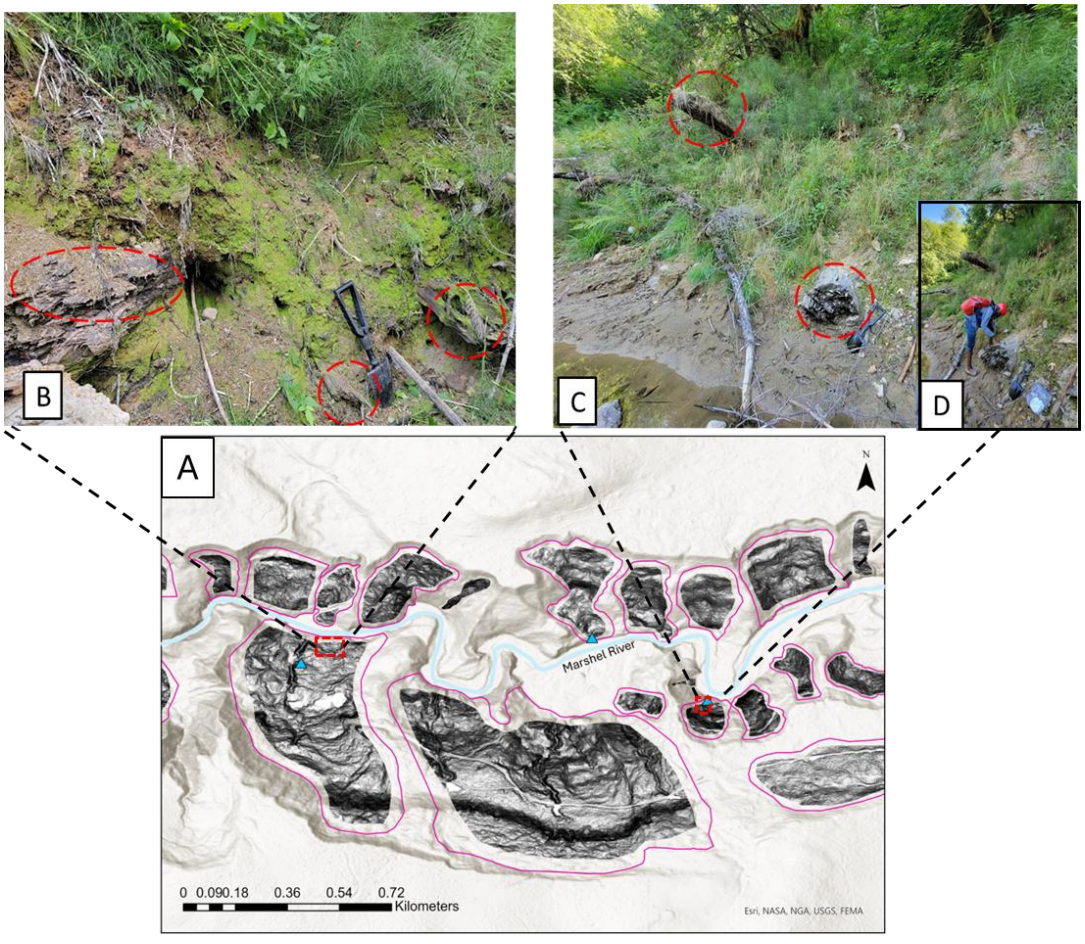


Figure 2(A) Hillshade map of mapped deep-seated landslides along the Marshiel River, with landslide polygons outlined in pink. Red boxes indicate field sampling locations shown in panels B–D. (B–C) Examples of stratigraphically constrained buried wood samples (red dashed circles) collected from landslide deposits. (D) Field sampling of buried log for radiocarbon dating. Base map: Esri World Hillshade (Esri, NASA, NGA, USGS, FEMA) | Powered by Esri.

## 2.3 Surface Roughness - Age Model

The use of surface roughness as a proxy for landslide age is based on the observation that landslide deposits are often roughest at the time of the landslide, as uneven movement on the slope creates jagged surfaces with angular orientation that smooths out with time as soil transport processes redistribute sediments, filling up pits and eroding mounds (McCalpin 1984). The continuous wavelet transform, a curvature-based metric, has been demonstrated to effectively quantify the

https://doi.org/10.5194/egusphere-2025-6555
Preprint. Discussion started: 30 March 2026


geomorphic degradation of landslide deposits across different spatial scales (Lahusen et al., 2016; Booth et al., 2017; Lai et al., 2025).

For this study, surface roughness was calculated for each landslide using the continuous wavelet transform (CWT) method with a 20 m Mexican Hat wavelet kernel, following Booth et al. (2017), Lahusen et al. (2020), and Underwood et al. (2025). Each landslide's roughness is defined as the mean of the absolute values of the curvature within the landslide polygon. Prior to analysis, each landslide polygon was carefully screened to exclude natural or modified areas that could introduce artificial roughness not attributed to diffusive soil transport. These included over-steepened toes, gullies, roads, buildings, and other anthropogenic features. The resulting roughness metric reflects the residual diffusive texture of each deposit.

We developed an empirical age-roughness model using the calibrated radiocarbon ages and corresponding surface roughness values of landslides of known age. Following the approach of Lahusen et al. (2016) and Booth et al. (2017), we applied non-linear regression to fit an exponential decay function to the observed age-roughness data. The model was then applied across the inventory of mapped landslides within glacial sediments to estimate their ages. Limiting the analysis to landslides within similar sedimentological contexts helped minimize the influence of variations in rock strength on landslide initial roughness and subsequent smoothing rate.

### 2.4 Landslide History Model

To assess whether trends in landslide frequency in the Puget Lowland exceed what would be expected from background processes alone at known times of paleoearthquakes, we developed a landslide history model. This was based on recent approaches by Lahusen et al. (2020) and Herzig et al. (2024), who introduced a probabilistic framework for reconstructing landslide frequency from age-inferred landslide inventories, incorporating preservation decay to account for diminishing visibility of older landslide deposits. LaHusen et al. (2020) noted that, owing to the nonlinear relationship between roughness and age, and the uncertainty in radiocarbon and roughness-inferred ages, an earthquake pulse in landslide history is most likely to present as a broad peak in landslide frequency. We adopt this approach but apply it to the study area in several keyways that differ from previous work. In this study, rather than focusing on a single fault, we apply this method to a larger spatial domain encompassing four Holocene active crustal fault

https://doi.org/10.5194/egusphere-2025-6555
Preprint. Discussion started: 30 March 2026


zones, including the Tacoma, Seattle, Southern Whidbey Island, and Darrington-Devils Mountain fault zones. Secondly, our model explicitly compares three scenarios: a steady-state model, a multi-fault earthquake model that incorporates landslide pulses at times of the most recent earthquakes in the four crustal faults, and single-event earthquake models for each individual fault zone. This multi-scenario structure allows us to evaluate the relative explanatory power of different triggering hypotheses. Third, while Herzig et al. (2024) developed separate models for both landslide frequency and area, we found that modeling area introduced distortions due to the outsized influence of a few very large landslides. While large-area landslides can persist in the landscape longer than smaller ones, landslide areas are not always indicative of event density. In contrast, number-based frequency modeling more reliably captured the temporal structure of landslide activity and was thus used exclusively in our study. Together, these applications enable a more spatially comprehensive and statistically controlled comparison of background and earthquake-influenced landsliding across the eastern Puget Lowland.

In the steady-state model, we assume a constant landslide rate for the Holocene. This constant background rate is modeled using an exponential decay function to reflect the progressive loss of landslide preservation over time (Booth et al., 2017; LaHusen et al., 2020; Herzig et al., 2024). This steady-state model captures background landslides, which we assume were mostly driven by non-seismic triggers, primarily rainfall. While we assume rainfall-induced landslides occur stochastically and are evenly distributed over time, this simplification does not fully account for prolonged or intense precipitation events. Strong storm events during heightened multi-year wet intervals, can produce widespread landsliding in the Pacific Northwest (Struble et al., 2021). This can result in short-term pulses in landslide frequency that may resemble seismic triggering signals. Such precipitation-driven peaks in landslide frequency introduce uncertainty into our interpretation, as some may reflect non-seismic sources. This limitation highlights the need for caution when attributing peaks in the landslide record to strong ground motion in the absence of supporting paleoseismic evidence.

In the multi-fault earthquake model, we simulate the impact of seismic triggering by introducing three discrete, time-bound pulses in landslide production. Each pulse is injected at the known and estimated timing of the most recent ruptures on the four fault zones in the Puget Lowland. These include a pulse at ~1100 ybp for the Seattle and Tacoma Fault (1027 ybp -Black et al., 2023; 930

https://doi.org/10.5194/egusphere-2025-6555
Preprint. Discussion started: 30 March 2026


- 1290 ybp - Bucknam et al., 1992; Sherrod, 2001; Nelson et al., 2008), ~2000 ybp for the Darrington–Devils Mountain Fault Zone (Personius et al., 2014), and ~3000 ybp for the Southern Whidbey Island Fault Zone (Kelsey et al., 2004). Each simulated pulse consisted of a sharp increase in landslide frequency, modeled as a fixed number of landslides added at each earthquake, and was superimposed on the same exponentially decaying background landslide rate used in the steady-state model to reflect preservation bias.

The multi-fault model was implemented as a composite simulation, meaning all three earthquake pulses were introduced within a single model run, rather than as separate simulations. This allowed us to evaluate whether a combined set of Holocene earthquakes across the region could account for the broad peaks observed in the landslide frequency curve. Because the Seattle Fault earthquake is the only event with high-precision age control, it provides the most robust target for comparison. The overlapping age ranges of the Tacoma and Seattle fault ruptures suggest the potential for an especially large landslide peak near ~1,000 ybp, whereas the older earthquakes on the DDMFZ and SWIFZ would be expected to generate more subdued signals due to both age uncertainty and greater preservation loss. These expectations serve as a basis for evaluating whether the simulated earthquake pulses align with subsequent patterns in the landslide frequency history.

To further explore this, we also simulated individual earthquake models for each fault zone, allowing us to compare their standalone fits with the multi-fault composite model. This comparative approach enables a more comprehensive evaluation of how each rupture scenario aligns with observed landslide frequency patterns. By comparing the output of these models with both the steady-state scenario and the roughness-inferred landslide inventory, we assess whether the compounded effects of multiple earthquakes provide a better fit to the long-term landslide record than individual earthquakes or background processes alone. The observed landslide frequency was reconstructed using roughness-derived age estimates and binned into 50-200 yr intervals.

### 2.5 Spatio-temporal Clustering Model

To assess the spatial distribution of landslides relative to Holocene-active fault structures in the Puget Lowland, we employed a spatial clustering model based on the Frequency Ratio (FR) method. Here, we attempt to unravel the influence of past seismic shaking on the spatial

https://doi.org/10.5194/egusphere-2025-6555
Preprint. Discussion started: 30 March 2026


distribution of deep-seated landslides in the Puget Lowland. This approach builds on previous work that applied bivariate statistical techniques to evaluate the spatial relationship between landslide occurrence and potential controls such as proximity to faults, slope, lithology, and hydrologic factors (Ozioko and Igwe, 2020; Ayalew et al., 2005; Lee and Pradhan, 2007). The FR method quantifies spatial association by comparing the proportion of landslides that occur within a given spatial zone to the proportion of the susceptible area that zone represents. Susceptible area is defined by a slope threshold, informed by our landslide inventory, to exclude regions with slope angles less than 10°. This thresholding ensures that the FR values are computed only over areas with demonstrable susceptibility to deep-seated landsliding. The FR method is expressed as:

$$FR = \frac{Landsldie\ Ratio}{Area\ Ratio} \quad (1)$$

Here, the Landslide Ratio is the number of landslides within a ring defined by two buffer distances from the fault, divided by the total number of landslides in the study area, while the Area Ratio is the susceptible area of that ring divided by the total susceptible area of the entire study site. A FR $> 1$ shows high landslide density per susceptible area in the given buffer distance, while FR $< 1$ suggests low landslide density per susceptible area within the buffer distance. We applied multiring buffers at 5-km intervals around each of the four fault zones, extending up to 25 km from each fault, dividing the study area into distance bands for subsequent spatial analysis.

To evaluate how landslide clustering varied through time, we temporally stratified the landslide inventory using roughness-derived age estimates and grouped the data into 300-year temporal bins. FR was calculated independently for each time slice, enabling assessment of temporal variability in spatial clustering relative to active fault traces. To statistically evaluate clustering patterns, we performed linear regression analyses of FR v. distance from the fault trace for each time bin and report the slope, its p-value, and $R^2$ to determine the direction and statistical significance of the observed clustering. Time slices with a significant negative slope with respect to distance from a particular fault were interpreted as evidence for spatial clustering near that fault. By applying this approach consistently across the four fault zones and time periods, we identified spatial clustering patterns that may reflect the timing and spatial extent of past seismic events.

https://doi.org/10.5194/egusphere-2025-6555
Preprint. Discussion started: 30 March 2026


## 3.0 Results

### 3.1 Landslide inventory

A total of 2,132 deep-seated landslides from the WGS landslide inventory, including refined complex failures, covering 8,444 km2 across the eastern half of the Puget Lowland, were used in this study. The mapped landslides are distributed throughout the region, with the highest concentrations occurring along bluff escarpments and along the margins of incised valley walls adjacent to major drainage channels (Fig. 1). These zones represent areas where topographic relief is greatest and where landslide susceptibility is enhanced by fluvial undercutting, groundwater discharge, or past glacial erosion. The inventory is dominated by complex landslides, accounting for 69.2% of the total mapped population. These are characterized by a combination of rotational movement near the head scarp and downslope flow or translational behavior. Landslide flows and rotational failures account for 17.3% and 11.2%, respectively, while 1.6% of the mapped landslides are translational failures. Landslide planform areas span from 1,020 $m^2$ to 2.81 $km^2$, with a mean of 76,000 $m^2$. Minimum failure depths vary from 1.5 m to 269 m, with an average of 16.3 m. Minimum landslide volumes, estimated using minimum failure depth and planform area, range from 4,438 $m^3$ to 440 million $m^3$, with a mean of approximately 2.38 million $m^3$. Slope angles across the mapped deposits range from 6° to 63°, with a mean value of 29°, consistent with other inventories of deep-seated landslides in the study area Herzig et al., 2024).

To reconstruct the temporal distribution of deep-seated landslides across the Puget Lowland, we supplemented a compiled dataset of previously published sources with newly dated deposits (Table 1). From this study, eight samples were dated from five distinct landslides at three landslide sites (Fig. 1 & 2). At the Carbon River landslide, Sample CR01, collected from a partially buried tree trunk beneath a large boulder at the toe of the deposit, returned a calibrated age of 622 - 522 ybp (95% confidence interval (CI)), with a highest peak of 540 cal BP, which we interpret as the most likely age of the landslide. Sample CR05, taken from a wedged branch exposed in a spring channel farther upslope, yielded a calibrated age of 499 - 322 cal BP with a peak corresponding to 475 cal BP. The spatial proximity and relatively similar ages suggest they represent either a single landslide event or a closely spaced sequence of failures, in which case CR01 likely captures the initial slope failure, and CR05 brackets subsequent retrogression of the unstable slope. Since the most likely calibrated ages differ by only 65 years, that discrepancy could also reflect variability

https://doi.org/10.5194/egusphere-2025-6555
Preprint. Discussion started: 30 March 2026


in which growth rings were sampled or in whether the wood was killed directly by the landslide or was already dead at the time of failure. Given the near overlap in age uncertainty, both ages were used in the age-roughness model.

At Lynch Creek, two samples (LC01 & LC02), collected from two distinct buried logs near the toe of the deposit, produced calibrated ages of 554-507 and 265-22 cal BP. We interpret the younger age as likely reflecting a minor, localized stream bank failure or partial landslide reactivation. Hence, we report the most likely age of the landslide as 525 cal BP, based on the peak of the calibrated age PDF from LC01; LC02 was excluded from the model.

Four samples were collected at three landslide locations along the Marshel River (Fig. 2). Sample MR06, taken from an intact log resting at the toe of the deposit, yielded a calibrated age of 960 - 836 cal BP with a peak PDF of 960 cal BP (Fig. 2C). Sample MR07 was recovered from a firmly embedded log within the deposit about 2 m from the toe; it returned a calibrated age of 2724 - 2464 cal BP with a peak PDF of 2650 cal BP. Sample MR08a, derived from a tree trunk, yielded several distinct 95% confidence-calibrated age intervals ranging from 283 ybp to modern, with a peak at 270 cal BP. Sample MR08b, a branch located near sample MR08a, gave a modern age, suggesting possible contamination or delayed mortality. Although lidar imagery shows a portion of modern reactivation on the landslide, the uncertainty on the 270 cal BP places it within the near-modern range, so we retained the age for the entire landslide. We therefore adopted 960 cal BP, 2650 cal BP, and 270 cal BP as the most likely ages for MR06, MR07, and MR08a landslides, respectively, and retained those ages in the model.

To expand the age-roughness model, we incorporated radiocarbon-dated landslide events from previous studies in glacial sediments across the Puget Lowlands (Table 1). We included the precisely dated Hamma Hamma coseismic landslide 1026-1027 cal BP (923-924 CE) linked with the ~1026 ybp rupture of the Seattle fault (Black et al. 2023). From Lahusen et al. (2016), we included Headache Creek (6149 ± 130 cal BP, median ± 1sigma calibrated age range as reported in that study), Rowan (588 ± 64 cal BP), and an age from the Skaglund site reported in Booth et al. (2017) (233 ± 79 cal BP), alongside several unnamed deposits with ages ranging from 580 ± 45 to 1,243 ± 53 cal BP. From Herzig et al. (2024), we included four ages from North Issaquah

https://doi.org/10.5194/egusphere-2025-6555
Preprint. Discussion started: 30 March 2026


(830 ± 80 cal BP), Schmitz Preserve North (405 ± 85 cal BP), and Norway Hill landslides, which yielded two mid-Holocene ages of 1,345 ± 45 and 1,620 ± 80 cal BP, respectively.

Ages for the May Creek (359 Cal BP) and Schmitz Park E (7390 Cal BP) landslides(Herzig et al. 2024), were excluded due to their small areas (~16,000 and ~13,900 m², respectively), which meant that only a limited portion of the deposit remained for calculating roughness after buffering to exclude deposit flanks, toes, gullies, and anthropogenic disturbances (Supplementary Material), because we used a larger buffer in this study than Herzig et al. (2024). These small patches were not representative of the landslides' overall roughness and seemed to bias the roughness toward anomalously smooth values for May Creek ($0.011 m^{-1}$) and anomalously rough values for Schmitz Park ($0.02 m^{-1}$), relative to their calibrated ages, which significantly deviated from the expected roughness-age trend. We therefore interpret the anomalous mismatch between roughness-derived and caliberated ages for these two landslides as likely due to insufficient representative surface area for reliable roughness quantification. These outliers substantially degraded model performance, with the $R^2$ dropping from 0.88 to 0.35 when they were included. A sensitivity analysis including these samples is provided in the supplementary material (S3 & S4, Table S1). In total, the compiled radiocarbon dataset includes 18 landslide ages, 8 of which are new, spanning the late to early Holocene, with most events occurring within the last 3,000 years. Of these, 14 were retained for use in the age-roughness model based on stratigraphic clarity, calibration confidence, and lithologic consistency with the rest of the inventory.

Table 1: Radiocarbon age data

| Landslide Reference | Sample name | Short description | Location (Lat, Long) | Lab_ID | Radiocarbon Age | Age_error | 95% C.I. of calibrated age range(s) [cal. yrs B.P.] | Age used in age-roughness model [cal. yrs B.P.] |
|---|---|---|---|---|---|---|---|---|
| New Landslide Age (This Study) | | | | | | | | |

https://doi.org/10.5194/egusphere-2025-6555
Preprint. Discussion started: 30 March 2026


| | | | | | | | | |
|---|---|---|---|---|---|---|---|---|
| Carbon River Landslide | CR01 | Outer wood from tree trunk sticking out of the landslide deposit. | 47.038029°N, 122.037138°W | OS-17563535 | 540 | 15 | 555–522<br>622–613 | 540[1] |
| Carbon River Landslide | CR05 | Inner wood from tree trunk sticking out of the landslide deposit. | 47.037763 1°N, 122.0358 378° W | OS-17563636 | 385 | 15 | 499–442<br>357–332 | 475[1] |
| Lynch Creek Landslide | LC01 | Inner wood from tree trunk sticking out of the landslide deposit. | 46.881296°N, 122.242359°W | OS-17563737 | 510 | 15 | 544–514<br>549–507 | 525[1] |
| Lynch Creek Landslide | LC02 | Inner wood from tree trunk sticking out of the landslide deposit. | 46.881296°N, 122.242359°W | OS-17563838 | 125 | 15 | 146–22<br>265-217 | Not used in the model |
| Marshel River | MR06 | Outer wood from tree trunk sticking out of the landslide deposit. | 46.865016°N, 122.222594°W | OS-17564242 | 1,020 | 15 | 957–919<br>960–909<br>843–836 | 960[1] |

https://doi.org/10.5194/egusphere-2025-6555
Preprint. Discussion started: 30 March 2026


| | | | | | | | | |
|---|---|---|---|---|---|---|---|---|
| Marshel River | MR07 | Wood saple from a stump/branch wedged in the landslide deposit | 46.866680°N, 122.225820°W | OS-175648 | 2,490 | 15 | 2600–2493 | 2650[1] |
| Marshel River | MR08 | Trunk | 46.867010°N, 122.234510° | OS-175650 | 155 | 20 | 283-251<br>229-168<br>117-63<br>42 - present | 270[1] |
| (LaHusen et al. 2016) | | | | | | | | |
| Headache Creek landslide | na | Bark (intact tree trunk) | 48.286 N, -121.849 W | | 5371 | 28 | 6019-6278 | 6149[2] |
| Smoothest one | na | Wood | 48.274 N, -121.858 W | | 10,103 | 37 | 11414-11986 | 11,700[2] |
| Rowan | na | Wood (broken branch) | 48.272 N, -121.879 W | | 572 | 37 | 524-651 | 588[2] |
| Black et al.(2023) | | | | | | | | |
| Hamma | na | Stumps in growth position | 47.537N, -123.066W | | - | - | 1026 - 1027 | 1026[3] |

https://doi.org/10.5194/egusphere-2025-6555
Preprint. Discussion started: 30 March 2026


| | | | | | | | |
|---|---|---|---|---|---|---|---|
| Hamma | | | | | | | |
| Booth et al.,(2017) | | | | | | | |
| Skaglund | na | Wood | 48.267 N, -121.860 W | 253 | 29 | 154-312 | 233[2] |
| Unnamed landslide | na | Wood | 48.279 N, -121.864 W | 1330 | 31 | 1190-1296 | 1243[2] |
| Unnamed landslide | na | Wood | 48.280 N, -121.864 W | 557 | 26 | 535-625 | 580[2] |
| Herzig et al., (2024) | | | | | | | |
| North Issaquah Slide | | Charcoal | 122°2'39.47" W 47°33'36.725 "N | 903 | 22 | 750-910 | 830[2] |
| Schmitz Park N | na | Wood | 122°24'5.205 "W 47°34'36.04" N | 382 | 23 | 320-490 | 405[2] |
| Norway Hill | na | Wood | 122°12'24.437"W 47°44'58.484 "N | 1463 | 24 | 1300-1390 | 1345[2] |

https://doi.org/10.5194/egusphere-2025-6555
Preprint. Discussion started: 30 March 2026


| | | | | | | | |
|---|---|---|---|---|---|---|---|
| Norway Hill | na | Wood | 122°12'20.92"W 47°44'58.089"N | 1706 | 37 | 1540-1700 | 1620[2] |

[1] Is most probable calibrated age.

[2]Medain age of 1sigma calibrated age range as reported in previous studies.

[3]Precise age from tree rings

### 3.2 Age-Roughness Model and Inferred Age

To estimate the timing of the full suite of deep-seated landslides in our inventory, we developed an exponential decay model relating landslide age to surface roughness, constrained by radiocarbon-dated deposits across the Puget Lowland. The age–roughness relationship follows an exponential function of the form: Age = 183411.3 * exp(–276.1 * Roughness), which explains 88% of the variance (Fig. 3). To more comprehensively account for uncertainty in landslide age, a Monte Carlo simulation was conducted varying radiocarbon calibrated ages within their standard deviations to produce a distribution of exponential fits. The final model represents the median fit from 10,000 iterations, with a 95% confidence envelope derived from the standard deviation of simulated age estimates at each roughness value (Fig. 3). This envelope reflects combined uncertainty in the radiocarbon calibration, roughness quantification, and model fit, and is used to propagate error through the landslide age reconstruction. This age–roughness relationship was applied to over 2,000 mapped landslides in the Puget Lowland to estimate their relative timing and assess changes in landslide frequency through time.

The reconstructed landslide age distribution shows a strongly right-skewed pattern, with a high frequency of young landslides and a rapid decline in occurrence with increasing age. This distribution also follows an exponential decay, which we suggest reflects the influence of preservation bias, where younger failures retain sharp morphologic expression and are more easily mapped, while older landslides become eroded and smoothened by hillslope diffusive processes,

https://doi.org/10.5194/egusphere-2025-6555
Preprint. Discussion started: 30 March 2026


making them less likely to be identified by a mapper, or are overprinted by younger events. Other studies on landslides in Washington and Oregon have identified similar trends where observed landslide frequency decreases with age (Booth et al., 2017; LaHusen et al., 2016; Herzig et al., 2024; Underwood et al., 2025). These findings underscore the need to account for geomorphic preservation bias when interpreting temporal trends from landslide inventories.

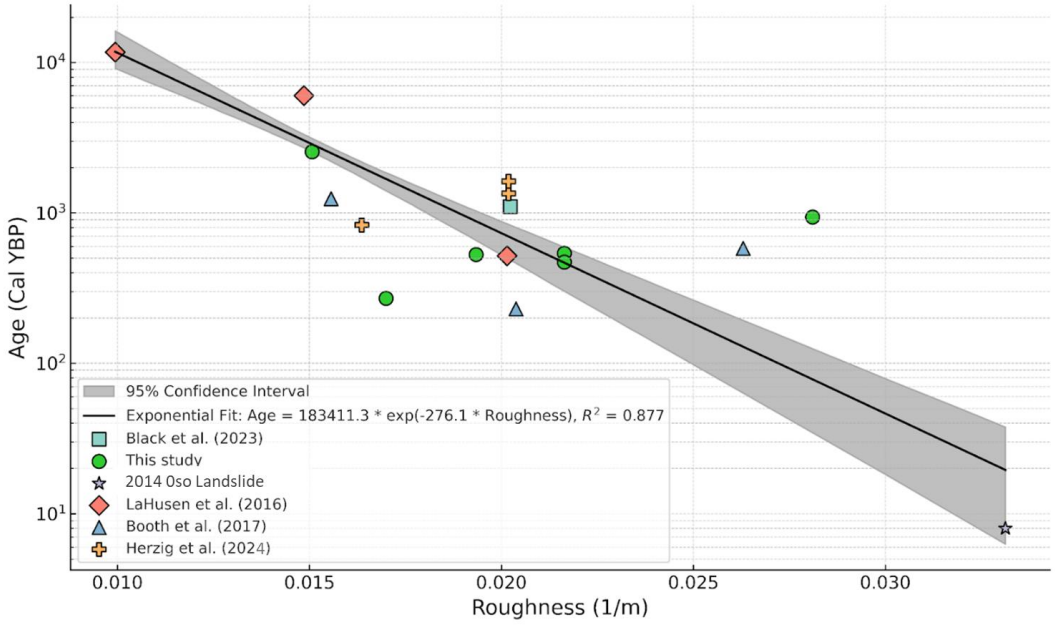


**Figure 3**: Landslide Age-Roughness model showing an exponential relationship between landslide age and roughness. The shaded gray region shows the 95% confidence interval on the fit, derived from 1000 Monte Carlo simulations that propagate uncertainty in both roughness and age.

### 3.3 Landslide History Model

The results of the modeled steady-state and multi-fault earthquake landslide scenario, overlaid with the observed landslide history derived from roughness-inferred landslide ages, are presented

https://doi.org/10.5194/egusphere-2025-6555
Preprint. Discussion started: 30 March 2026


in Figure 4. The results presented here are with 100 bins; results with 50, 150 and 200-year bins are presented in the supplementary material. Periods in which this curve significantly exceeds the steady-state model, defined here as those above the 90th percentile of the synthetic steady-state distribution across 10,000 Monte Carlo runs, indicate possible landscape responses to external forcing beyond background expectations. To mitigate the influence of preservation bias and the overrepresentation of younger landslides in the inventory, we excluded landslides younger than 150 years from our model. Informed by the post-150 ybp landslide rate, the steady-state and earthquake models were set to 0.72 landslides per year.

To test whether multiple Holocene earthquakes contributed to episodic increases in landslide frequency, we compared the observed chronology against the multi-fault earthquake model described in the methods. That model incorporates pulses associated with the Seattle-Tacoma, Darrington-Devils Mountain, and Southern Whidbey Island fault zones, superimposed on the same exponentially decaying background used in the steady-state scenario. Guided by rmsle, the best-fit steady-state and multi-fault models both approximate the overall decay trend of the landslide inventory.

https://doi.org/10.5194/egusphere-2025-6555
Preprint. Discussion started: 30 March 2026


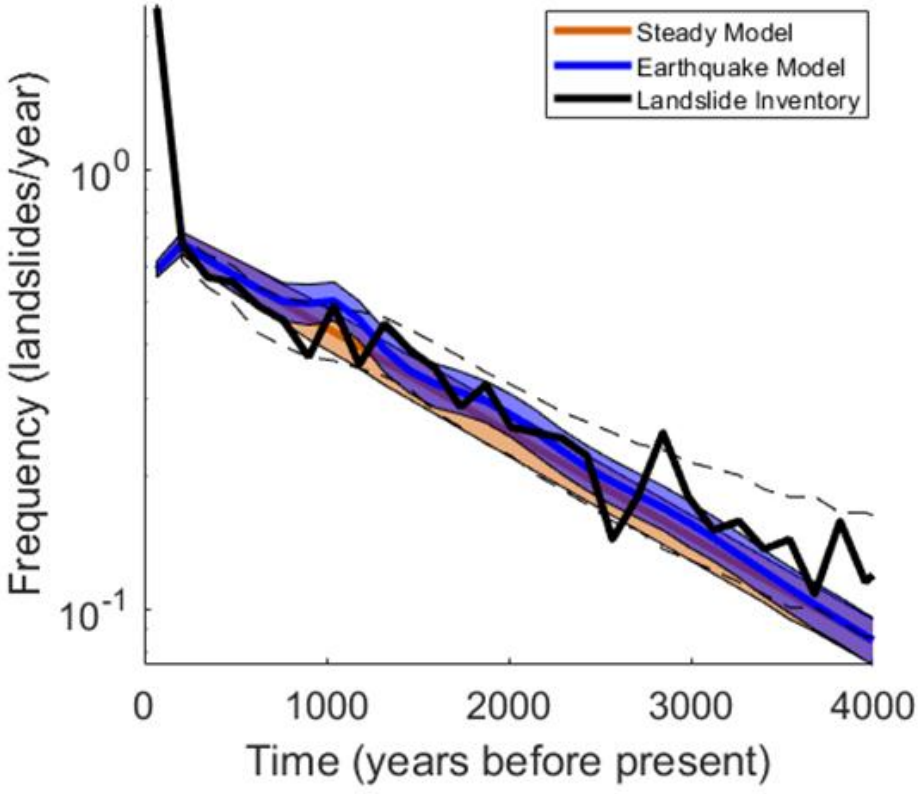


538

539 Figure 4: Landslide frequency v. time before present grouped into 100-yr bins for steady-state
540 (brown) and multi-fault earthquake model (blue) overlayed on the observed landslide frequency
541 (black). The dashed grey lines indicate the 2σ uncertainty bounds.

542

543 Results from the steady-state and multi-fault earthquake models (Fig 4) both reproduce the overall
544 trend in observed landslide frequency over time, as the observed frequency largely falls within the
545 confidence bounds of both modeled histories. However, the observed frequency exceeds the
546 confidence bounds of the steady model at ~1000 ybp, 1250 ybp, 1900 ybp, and 2800–3200 ybp,
547 suggesting temporal clustering of landslides during these intervals. These peaks correspond with
548 pulses in the multi-fault earthquake model history at ~1100, ~2000, and ~3000 ybp, respectively,
549 supporting the interpretation that multiple Holocene earthquakes contributed to these elevated
550 periods of landsliding. Within the earthquake model, the simulated pulse at 1100 ybp stands out

https://doi.org/10.5194/egusphere-2025-6555
Preprint. Discussion started: 30 March 2026


as a well-defined peak, reflecting the timing of the Seattle-Tacoma rupture. By contrast, the older simulated pulses at 2000 and 3000 ybp appear more subdued and less distinct due to larger absolute age uncertainties of the older landslides. Although the observed history exhibits two closely spaced peaks at ~1000 and ~1250 ybp, these peaks closely overlap earthquake timing in the Seattle and Tacoma Fault zones.

Relative to the observed landslide history, the multi-fault model yielded an rmsle of 0.0397 yr-1, slightly outperforming the steady-state model, which returned an rmsle of 0.0399 yr-1. With a slightly improved rmsle, the multi-fault model provides a better reconstruction of temporal fluctuations in landslide frequency, particularly the distribution of landslide clusters near 1100 ybp, 1900 ybp, and 2800–3200 ybp, which broadly corresponds to the timing of major Holocene earthquakes in the Puget Lowland.

Additionally, to explore the influence of individual fault ruptures on the landslide distribution, we developed single fault models (Supplementary material (S5-S9) centered on the approximate timing of earthquakes on the TFZ, SFZ, SWIFZ, and DDMFZ. These simulations yielded rmsle values of 0.0427 yr-1 for the SFZ (1027 ybp), 0.0414 yr-1 for the TFZ (1100 ybp), 0.0390 yr-1 for the SWIFZ (3000 ybp), and 0.0391 yr-1 for the DDMFZ (2000 ybp). The SWIFZ and DDMFZ earthquake simulations, with lower rmsle values than the multifault model, provide a stronger fit to localized peaks in the landslide record at 3000 and 2000 ybp, respectively, and lack a clear peak at 1000 ybp. This comparison highlights that while the single-fault models reproduce individual peaks in landslide frequency that coincide with their respective rupture ages, they do not account for the full range of observed clustering. By contrast, the multi-fault model incorporates pulses from all four major crustal faults and therefore provides a more comprehensive match to the observed chronology, reproducing broad peaks that overlap observed clusters ~1000-1300, ~1800-2200, and ~2800-3200 ybp. Given the cumulative uncertainty in landslide dating, roughness-age calibration, and preservation bias, the multi-fault model remains consistent with the observed inventory and provides a tectonically informed explanation for temporal clustering that is not accounted for by background landsliding alone. While the steady-state and multi-fault earthquake models yield nearly identical RMSE values (0.0399 and 0.0397, respectively), and two of the single-fault simulations (DDMFZ and SWIFZ) individually outperform the multi-fault model, we adopt the multi-earthquake model because it best captures the broader spatiotemporal trends in the

https://doi.org/10.5194/egusphere-2025-6555
Preprint. Discussion started: 30 March 2026


landslide record and offers a more tectonically reasonable explanation for Holocene clustering across the entire region.

However, while the modeled earthquake-triggered pulses broadly align with elevated periods in the observed landslide frequency curve, the correspondence is not perfect. Some peaks in the observed record are offset from the simulated pulse timings, and their prominence can vary with the chosen bin width, introducing interpretive uncertainty. These subtle mismatches highlight the limitations of relying solely on temporal comparisons to infer seismic triggering. To better resolve the signal of individual earthquakes, we therefore extend our analysis to consider both the spatial distribution of landslides and their proximity to mapped fault traces. This spatiotemporal approach provides an additional line of evidence to evaluate whether specific faults are associated with observed periods of landslide clustering.

### 3.4 Spatio-temporal clustering

Frequency-ratio results from all four fault zones reveal varying evidence for spatial clustering of landslides near faults. These patterns, when temporally constrained to 300-year time bins, provide a framework for assessing whether fault-specific seismic events may have influenced past landslide activity. Specifically, we expect to see an increase in landslide frequency that decays away from the fault trace during the known earthquake window.

The Tacoma Fault Zone (TFZ) has an increasing landslide-susceptible area ratio with distance from the fault, increasing from 13.5% at 5km to about 32% at the 25 km distance class (Fig.5). Landslide frequency for most time slices exhibits a bimodal pattern with high landslide frequency either near or far from the fault. Specifically, in half of the time slices, fault proximity controls landslide clustering; in the other half, susceptible area percentage controls landslide location. This is confirmed by the Frequency Ratio (FR) analysis, which reveals consistently elevated levels of landslide occurrence within 5–10 km of the fault across 8 of the 12 calibrated time slices. Time intervals of 300-1800 and 2400-2700 ybp exhibit negative slopes in FR v. distance from fault, consistent with fault-proximal control on landslide clustering, whereas 1800-2400 and 2700-3900 ybp display mostly positive slopes, coincident with higher concentrations away from the fault. Although none of these negative trends are statistically significant at the 95% confidence level (Table S1), the 900-1200 and 1200-1500 ybp time slices recorded the highest $r^2$ values of 0.61 and

https://doi.org/10.5194/egusphere-2025-6555
Preprint. Discussion started: 30 March 2026


610 0.59, respectively. These slices broadly envelop the timing of the last earthquake on the TFZ. The
611 other salient feature of FR analysis is the high concentration of landslides around 20 km of the
612 fault outside known earthquake windows. This heightened landslide density reflects the influence
613 of local geomorphic and hydrologic conditions rather than proximity to fault or coseismic ground
614 motion.

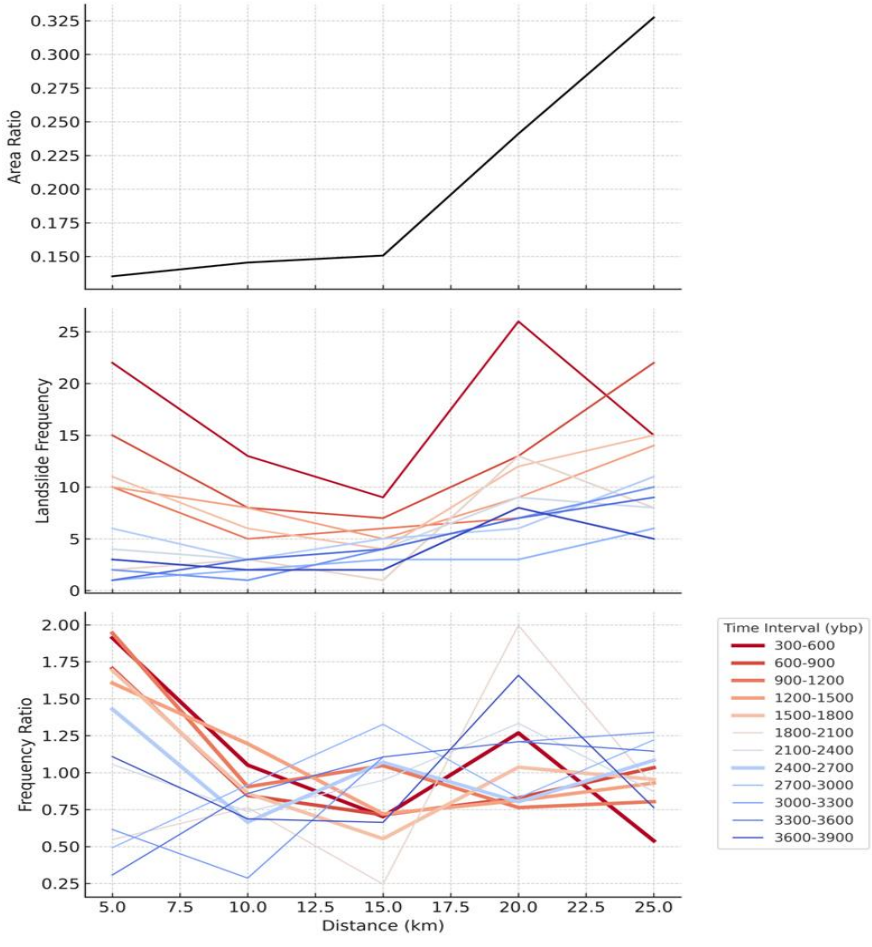


615

616 Figure 5: Spatial distribution of landslide Susceptible area (top), frequency (middle) and FR
617 (bottom) with respect to distance from the TFZ. FR intervals with negative slopes (landslide
618 frequency decreases away from the fault) are highlighted by thick lines.

619

https://doi.org/10.5194/egusphere-2025-6555
Preprint. Discussion started: 30 March 2026


The Seattle Fault Zone (SFZ) (Fig. 6) exhibits a clear spatial pattern of landslide clustering over the past 4000 years, underscoring strong fault-proximal control on landslide occurrence. The susceptible area ratio within the defined buffer distances increases progressively from approximately 12.4% at 5 km to about 21.4% at 25 km. Landslide frequency in those susceptible areas does not systematically change with distance, regardless of time interval. However, frequency Ratio (FR) analysis consistently reveals elevated landslide occurrence within 5 km of the fault across all analyzed intervals, except the 3000-3300 ybp interval. All time intervals except 3000-3300 ybp exhibit negative slopes, highlighting a persistent pattern of decreasing landslide concentration with increasing distance from the fault. These negative slopes strongly suggest fault-proximity control on landslide clustering, with particularly pronounced trends within the 600–900 ybp (slope = -0.0447 km-1; $R^2 = 0.97$; p(slope) = 0.003), 1200–1500 (slope = -0.0410; $R^2 = 0.92$; p(slope) = 0.010), and 1800–2100 (slope = -0.0901; $R^2 = 0.95$; p(slope) = 0.005) respectively.

The Southern Whidbey Island Fault Zone (SWIFZ) (Fig. 7) also shows a predominantly fault-proximal spatial pattern of landslide clustering, characterized by subtle yet consistent negative slope trends in most analyzed time intervals. The susceptible area ratio steadily increases from approximately 13.5% at the closest buffer distance of 5 km to about 32% at the furthest buffer of 25 km, indicating progressively greater availability of susceptible terrain further from the fault. This trend is corroborated by the landslide frequency, which appears to increase progressively from the inner buffers to the outermost buffer classes. However, negative slope trends in FR values observed 600–900, 1200–1500, 2400–2700, 3300–3600, and 3600–3900 ybp instead indicate modest decreases in landslide concentration with increasing distance from the fault. The interval 1200–1500 ybp shows the strongest fault-proximal control, with a statistically significant negative slope (-0.0225, p-value = 0.010) and a high $R^2$ value (0.92). None of the observed negative trends seems to overlap with the last known earthquake (~3000 ybp) in the SWIFZ.

https://doi.org/10.5194/egusphere-2025-6555
Preprint. Discussion started: 30 March 2026


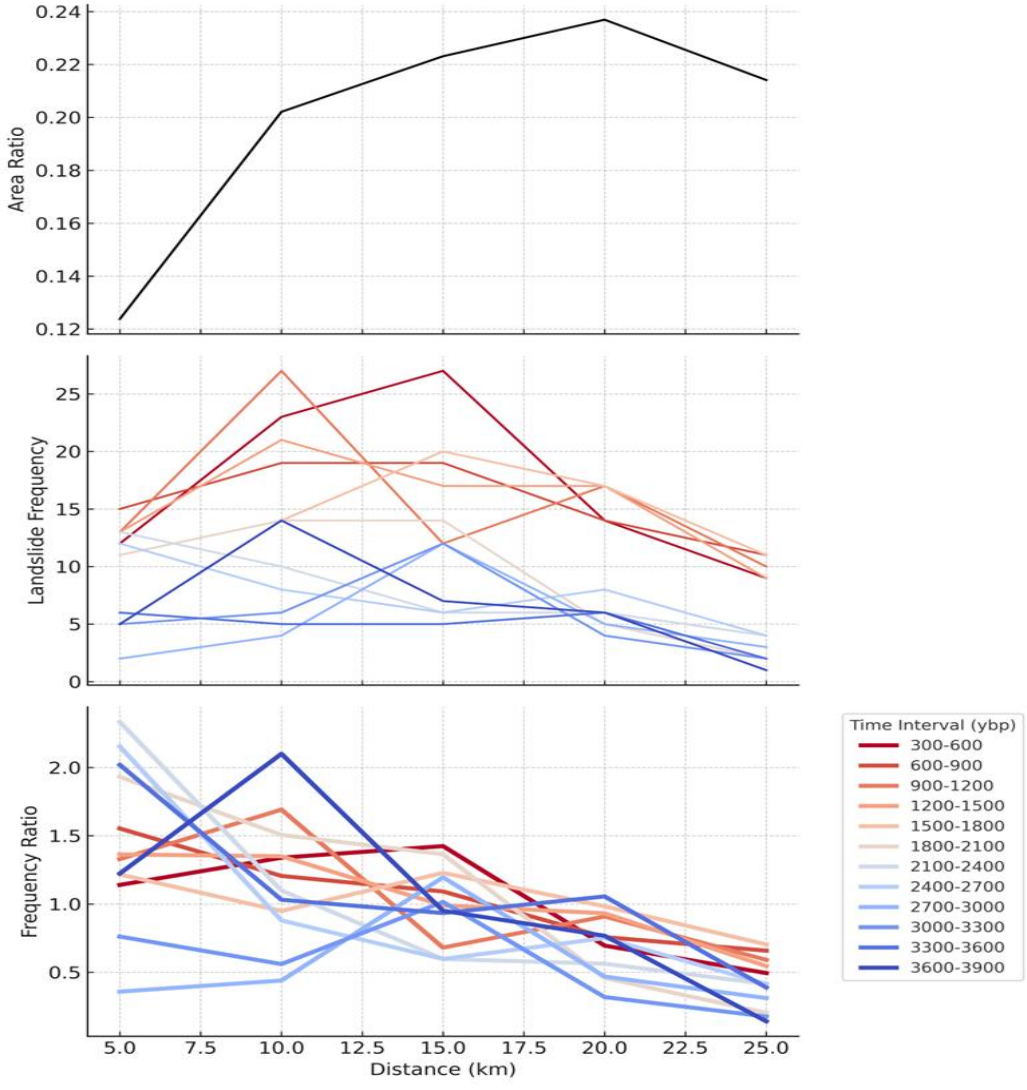


Figure 6: Spatial distribution of landslide Susceptible area (top), frequency (middle) and FR (bottom) with respect to distance from the SFZ. FR intervals with negative slopes are highlighted by thick lines.

https://doi.org/10.5194/egusphere-2025-6555
Preprint. Discussion started: 30 March 2026


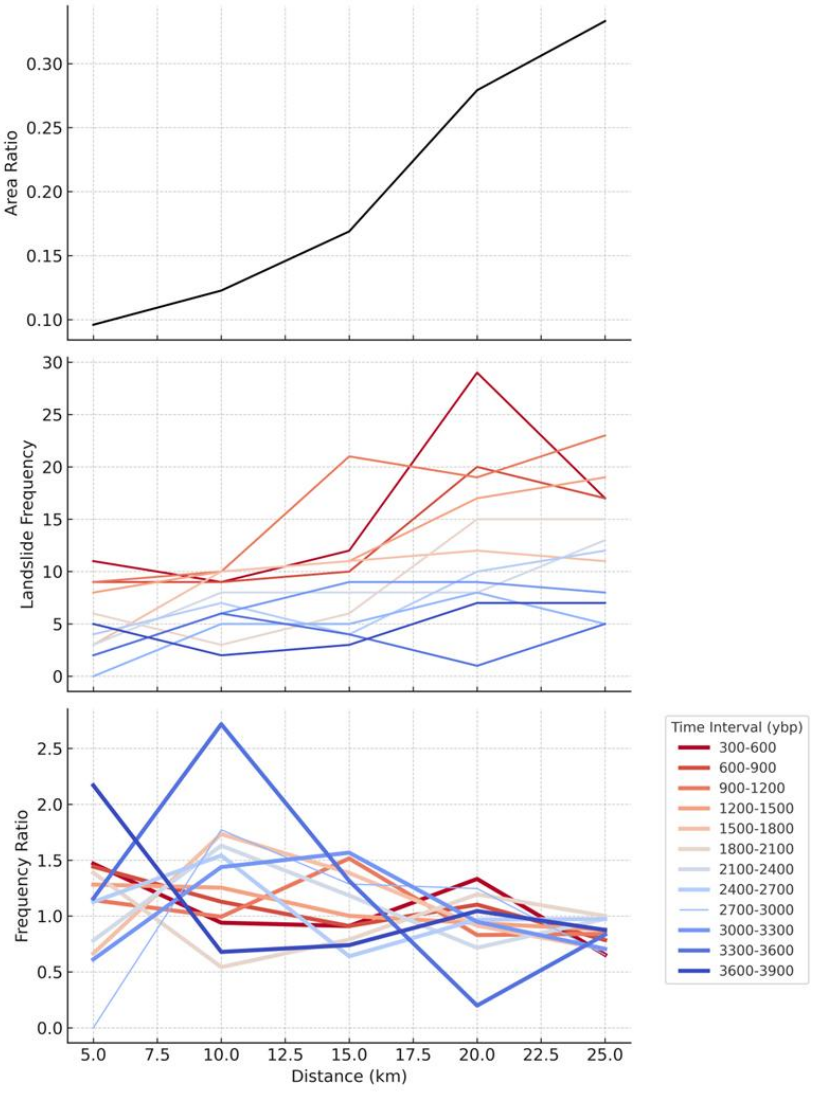


650

651 Figure 7. Spatial distribution of landslide susceptible area (top), frequency (middle) and FR
652 (bottom) with respect to distance from the SWIFZ. FR intervals with negative slopes are
653 highlighted by thick lines.

654

655

https://doi.org/10.5194/egusphere-2025-6555
Preprint. Discussion started: 30 March 2026


The Darrington–Devils Mountain Fault Zone (DDMFZ) (Fig. 8) exhibits a remarkably strong and persistent pattern of landslide clustering near the fault trace across nearly all time intervals. Unlike the other fault zones analyzed, the susceptible area ratio decreases with distance from the fault, dropping from approximately 36.5% at 5 km to about 11.6% at 25 km. Landslide frequency and Frequency Ratio (FR) values both consistently peak within the 5 km distance class, with FR values exceeding 1.0 in 10 of the 12 analyzed time intervals. Time slices of 900–1200, 1200–1500, and 3300–3600 ybp show particularly high near-fault FR values of 2.06, 2.06, and 2.19, respectively. The 600–900 ybp interval yields the strongest regression fit (slope = –0.0788; $R^2$ = 0.78; p = 0.047), supporting a statistically significant decline in landslide frequency with increasing distance from the fault. Similar to the SWIFZ, none of these intervals overlap with the timing of the most recent rupture of the DDMFZ.

https://doi.org/10.5194/egusphere-2025-6555
Preprint. Discussion started: 30 March 2026


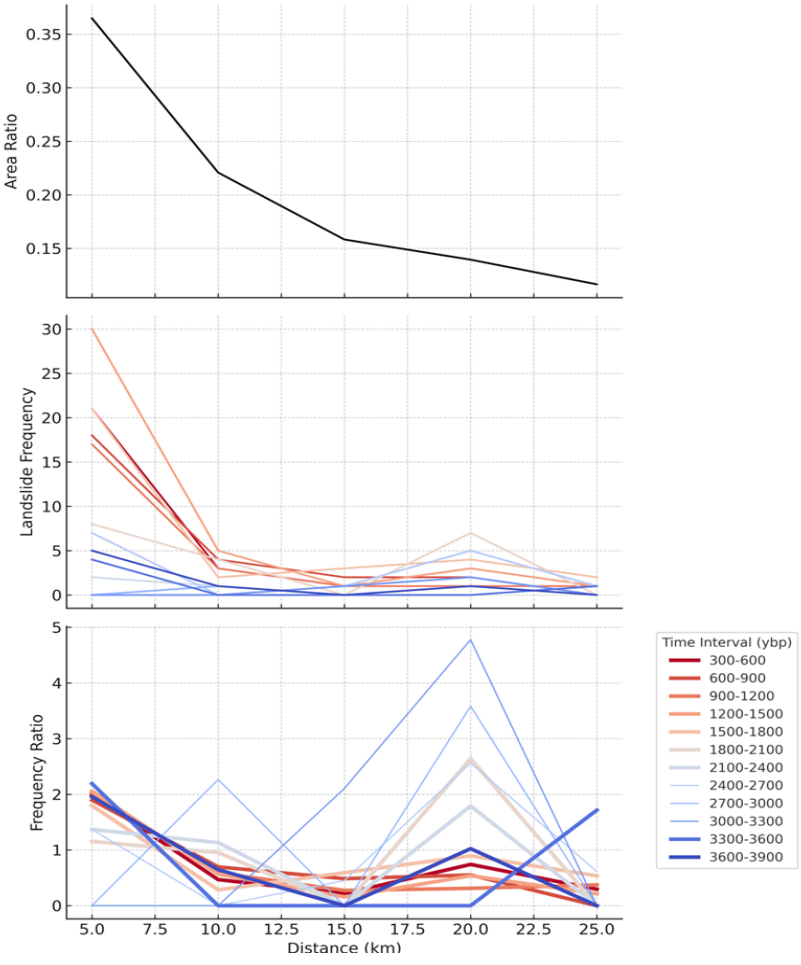


Figure 8. Spatial distribution of landslide susceptible area (top), frequency (middle) and FR (bottom) with respect to distance from the DDMFZ. FR intervals with negative slopes are highlighted by thick lines.

These results indicate that spatial clustering of landslides near fault traces is detectable in multiple time intervals across the study area. The nature of these patterns varies by fault and by time slice. Still, several intervals exhibit significant spatial characteristics consistent with fault-proximal landsliding, potentially triggered by strong ground shaking. Specifically, clustering is most pronounced along the Seattle Fault Zone at 600-900, 1200-1500, and 1800-2100 ybp; along the Tacoma Fault Zone at 900-1500 ybp; along the Darrington-Devils Mountain Fault Zone at 900-

https://doi.org/10.5194/egusphere-2025-6555
Preprint. Discussion started: 30 March 2026


1200, 1200-1500, and 3300-3600 ybp; and along the Southern Whidbey Island Fault Zone at 1200-1500 ybp. These temporal signals provide a basis for further interpretation in the following section, where they are compared against known Holocene earthquake chronologies.

## 4.0 Discussion

The landslide chronology developed in this study provides a comprehensive reconstruction of Holocene slope instability in the Puget Lowland. Our results show broad clusters in the distribution of deep-seated landslides that temporally overlap the most recent earthquakes on the four crustal faults under study. Two peaks at ~1000 and ~1200 ybp overlap with the timing of the Seattle fault and Tacoma fault earthquakes (1027 ybp and 830-1290 ybp, respectively). This result corroborates the findings of Herzig et al. (2024), who show a peak in landslide frequency coincident with the last SFZ earthquake. This supports the interpretation that the ~1000 ybp events on these faults contributed to an interval of heightened regional landslide activity. Additional peaks near ~2000 ybp and ~3000 ybp align with the most recent ruptures on the Darrington–Devils Mountain and Southern Whidbey Island fault zones, respectively. This further indicates that multiple large earthquakes have influenced slope stability across the Holocene landscape of the Puget Lowland. Although uncertainties in roughness-based ages preclude precise event-scale correlations, the temporal patterns are consistent with episodic, earthquake-driven pulses of mass wasting superimposed on a steady background rate of landsliding.

On the other hand, uncertainties from radiocarbon dating and roughness calibration influence the interpretation of results. Landslide age derived from radiocarbon can be younger or older than the landslide event. This results when sampled materials are from reworked wood or long-resident charcoals that produce ages likely older than the landslide event. Conversely, reactivation and mixing from bioturbation can introduce younger materials that may reflect the age of the latest activity on a portion of the landslides but not the initial failure event. Surface roughness often captures the most recent phase of activity on a landslide, whereas radiocarbon samples may capture any phase of landslide movement, including slow creeps, intermittent reactivations over millennia (Booth et al., 2017; Pánek, 2014). This fundamental potential for mismatch helps explain variability in the roughness-age relationship. Roughness is also influenced by failure style (McKean and Roering, 2004; McCalpin, 1984 ); e.g., rotational slides tend to preserve rough

https://doi.org/10.5194/egusphere-2025-6555
Preprint. Discussion started: 30 March 2026


morphology longer than flows. Localized reactivation of a dormant landslide would rejuvenate roughness for the reactivated area without resetting the full deposit roughness and, consequently, would impact the inferred age. Additionally, the roughness pre-processing shrinks the total deposit area available for the final roughness computation. This means that landslides with a small areal extent may be assigned roughness values that are not representative of the majority of the deposit surface, making them prone to outlier effects. In summary, these uncertainties suggest that our landslide chronology is best interpreted as a regional signal that captures broad temporal clusters rather than the precise occurrence of individual events. However, by combining radiocarbon control with preservation-corrected simulations, the model provides a robust framework for distinguishing peaks in landslide frequency plausibly linked to Holocene earthquakes from background activity.

The combination of landslide chronology and spatial proximity analyses reveals a nuanced pattern of potentially earthquake-triggered landslides across the Puget Lowland. Although the regional landslide history includes signals that align with multiple Holocene fault ruptures, the strength and clarity of these signals vary substantially among the studied fault zones. Notably, while our synthetic models show the best statistical fit in a multi-fault scenario, in single-fault simulations, the TFZ and SFZ show good statistical fits but are slightly outperformed by the steady-state model. We attribute this to the temporal proximity of rupture timing between the TFZ and SFZ, which makes it difficult to isolate the landslide response of each fault individually, as associated peaks in landslide frequency overlap within the uncertainty range of our age-roughness model. Consequently, failure triggered by one event may appear as part of a composite cluster rather than a distinct pulse, diminishing the statistical advantage of the single-fault model for these faults. In effect, we infer that the TFZ and SFZ signals are superimposed both temporally and spatially, producing a regional pulse that is better represented by the multi-fault model. On the other hand, the single-fault models of the DDMFZ and SWIFZ outperform the steady-state model, offering compelling evidence that the broad peaks in landslide frequency overlapping the ~2000 and ~3000 ybp earthquake windows on the DDMFZ and SWIFZ were at least partly seismically influenced. This observation echoes results from Herzig et al. (2024), who found that compared to the steady-state model, the earthquake model better explained temporal peaks in landslide history coincident with the last rupture of the SFZ. Furthermore, since these temporal peaks reflect landslides found throughout the study area, not just near these fault zones, our result suggests strong shaking from

https://doi.org/10.5194/egusphere-2025-6555
Preprint. Discussion started: 30 March 2026


these earthquakes may have occurred throughout the Puget Lowland, a finding corroborated by USGS scenario Shakemap models for the TFZ, SFZ, SWIFZ and the DDMFZs, which predict basin-wide amplification and high peak ground velocities across the region (USGS, 2022a, 2022b, 2022c; Washington Geological Survey, 2021).

This study extends this inference across a broader set of crustal faults and improves model precision using a larger, roughness-calibrated landslide inventory and tighter radiocarbon age control. However, the broad rather than sharp temporal peaks that coincide with known earthquake ages suggest that the landslide record integrates multiple competing influences. Preservation bias likely obscures older events, while regional averaging and background triggers blur signals from more recent earthquakes. These uncertainties underscore the need for spatial analysis, where local clustering can be evaluated more directly against fault proximity.

The spatial clustering of landslides across the TFZ, SFZ, SWIFZ, and DDMFZ reveals both shared patterns and distinct contrasts that reflect interactions between geomorphic susceptibility, seismic forcing, and landscape history. In the TFZ, SFZ, and SWIFZ, the proportion of landslide-susceptible terrain increases with distance from the fault trace, with the lowest percentage (as little as 13.5%) near the fault and the highest (up to 32%) at 25 km. This outward distribution suggests that, in absolute terms, landslides should occur preferentially farther from faults. However, frequency ratio (FR) values indicate that relative landslide densities remain consistently elevated within 5-10 km of the faults, suggesting that tectonic controls often override the background susceptibility. In contrast, the DDMFZ exhibits a reversed pattern, with the highest concentration of susceptible terrain adjacent to the fault (36.5% at 5 km, decreasing to 11.6% at 25 km). This geometry amplifies clustering near the fault, likely driven by persistent geomorphic instability in the North Fork Stillaguamish Valley, where deep glacial stratigraphy, outwash cover, and lateral river incision promote slope failure (Booth et al., 2017; Perkins et al., 2017).

Evidence for coseismic and post-seismic landsliding is most clearly expressed in the TFZ and SFZ. In the TFZ, the 900-1200 and 1200-1500 ybp time slices fall within or closely bracket the timing of the most recent earthquake (930-1290 ybp; Sherrod et al., 2004; Nelson et al., 2008), and both intervals exhibit strong negative trends in FR v. distance from fault ($R^2$ = 0.61 and 0.59, respectively), suggesting a direct coseismic landslide response. Additionally, we interpret the

https://doi.org/10.5194/egusphere-2025-6555
Preprint. Discussion started: 30 March 2026


persistence of fault-proximal clustering in the 600-900 and 300-600 ybp time slices to likely reflect a post-seismic legacy effect, in which marginally stable hillslopes destabilized by strong ground motion failed in the centuries that followed. Such delayed responses have been observed in other tectonically active regions, typically on the scale of years to decades following major earthquakes, although such studies have mainly focused on shallow landslides (Fan et al., 2019; Crozier, 2010). The much longer time spans observed here may therefore represent a broader geomorphic legacy of Holocene earthquakes in the Puget Lowland, potentially amplified by regional factors such as weak glacial stratigraphy, high-intensity precipitation events, and repeated reactivation of large landslide complexes. Similarly, in the SFZ, statistically significant fault-proximal trends in the 600-900 ybp ($R^2 = 0.97$; $p = 0.003$) and 1200-1500 ybp ($R^2 = 0.92$; $p = 0.010$) slices bracket the timing of the well-documented 1026-1027 ybp earthquake (Black et al., 2023). An additional significant trend occurs in the 1800–2100 ybp interval ($R^2 = 0.95$, $p = 0.0052$), suggesting a separate cluster of fault-proximal landsliding that may correspond to older Holocene seismicity. This interval broadly overlaps with a 2000 -2200 ybp landslide cluster (Herzig et al. 2024) that could be indicative of an older seismic event on the SFZ.

The observed landslide chronology shows two main peaks, at roughly 1000 ybp and 1200 ybp. These peaks overlap the timing of the 1026-1027 ybp SFZ earthquake and the 930-1290 ybp TFZ earthquakes (Black et al., 2023;Bucknam et al., 1992; Sherrod, 2001; Nelson et al., 2008). This correspondence suggests that both earthquakes may have contributed to the elevated landslide activity during this period. On the other hand, age-roughness models carry relative age uncertainties on the order of several tens of percent and may be biased if the sample of directly dated landslides is systematically rougher or smoother than the general population of landslides (Booth et al., 2017; Herzig et al., 2024; Underwood, 2025). As such, it is reasonable to interpret either of these two peaks as plausibly recording a geomorphic response to the TFZ or the SFZ event. This alignment supports the broader hypothesis that crustal earthquakes leave detectable spatial imprints in the landslide record, even when susceptibility near the fault is low. We therefore suggest that landslide density should be normalized by the area susceptible to landslides when using paleolandslides as indicators of paleoseismicity.

In contrast, the SWIFZ rupture (~2800-3200 ybp; Kelsey et al., 2004; Sherrod et al., 2008) leaves only a weak signature in the landslide record. The ~3000 ybp time slice shows no notable increase

https://doi.org/10.5194/egusphere-2025-6555
Preprint. Discussion started: 30 March 2026


in clustering near the fault, potentially due to preservation bias and the large absolute age uncertainties of roughness-based dating in the older landslide sample. Older landslides are more likely to be eroded, buried, or reactivated (Booth et al., 2017; LaHusen et al., 2020). While preservation correction was applied, subtle signals, such as the ~3000 ybp SWIFZ rupture, may still be difficult to systematically detect. Interestingly, the strongest clustering in the SWIFZ occurs in the 1200–1500 ybp interval ($R^2 = 0.92$), which may reflect a different seismic source or a period of heightened regional instability due to other preconditioning and triggering factors.

Although the ~2000 ybp earthquake on the DDMFZ (Personius et al., 2014) temporally aligns with elevated landslide activity in the 1800-2400 ybp window, the highest FR values during this interval occur at 20 km from the fault, rather than within the 5 km zone. Four of the seven landslides (57%) that drive this 20 km peak are located along Canyon Creek and the South Fork Stillaguamish River, valleys that are entrenched in weak glacial outwash, till, and lacustrine units. Similar processes in the North Fork Stillaguamish have been shown to sustain Holocene landslide activity independent of seismic forcing (Booth et al., 2017; Lahusen, 2016), suggesting that this signal may reflect localized geomorphic controls, such as river undercutting and reactivation of preexisting instabilities, rather than a coseismic response. On the other hand, the highly susceptible 0–5 km zone lies within the narrow valley of the North Fork Stillaguamish River, a reach that is especially prone to landsliding due to incision into thick glacial deposits. FR values show elevated landslide frequency post-~2000 ybp, increasing the likelihood of overprinting by coseismically triggered failures. In older time slices, the few, sporadic landslides mapped produced elevated FR values at certain distances and time intervals. These peaks are best interpreted as artifacts of small sample size rather than evidence of localized triggering.

Several key factors complicate the interpretation of these spatial signals. A major interpretive challenge arises when geomorphic susceptibility and fault proximity co-occur. Thrust-fault uplift and associated fault scarps create steep terrain that is naturally prone to landslides, making it difficult to isolate long-term tectonic forcing from true coseismic effects. Yet, in the TFZ and SFZ, high landslide activity near the fault, despite low proximal susceptibility, strongly suggests a tectonic signal. However, high FR values near the DDMFZ might suggest fault-proximal control; it is important to recognize that these valleys also contain large areas of highly susceptible terrain within 5km of the fault trace. Because FR already normalizes for susceptible areas, elevated values

https://doi.org/10.5194/egusphere-2025-6555
Preprint. Discussion started: 30 March 2026


imply more failures than expected. However, given the complexity of glacial stratigraphy and valley incision, it is difficult to separate coseismic forcing from the terrain's geomorphic predisposition. Thus, high FR should not be interpreted as evidence of fault control alone, but rather as the outcome of both seismic and non-seismic influences. This overlap complicates efforts to isolate coseismic landslide signals in geomorphically predisposed settings. Secondly, preservation bias makes it difficult to detect older landslides, as the probability of survival declines over time (LaHusen et al., 2020). This likely explains the muted response to the SWIFZ and the DDMFZ rupture.

Lastly, temporal overlap between nearby fault ruptures poses a significant challenge for attributing landslides to individual seismic events. The TFZ and SFZ ruptures occurred within a few decades of each other, and given the uncertainties in roughness-derived ages that exceed that time range (Lahusen et al. 2016; Booth et al., 2017; Herzig et al., 2024; Underwood, 2025), landslides triggered by either event may exhibit overlapping ages. This overlap complicates efforts to distinguish coseismic signals from each fault. Moreover, the earlier TFZ rupture may have depleted many marginally stable slopes in the region, leaving fewer failures to occur when the SFZ subsequently ruptured. This kind of inter-fault interaction, in which sequential strong ground motion alters slope thresholds and reduces the available unstable terrain, has been documented in other tectonically active mountain belts (Dadson et al., 2004; Lin et al., 2008; Hovius et al., 2011). Together, these factors underscore that roughness-based reconstruction of the coseismic landslide chronology is best suited to settings with isolated rupture events, where the geomorphic response is less likely to be confounded by overlapping seismic influences or compounded by slope-depleting effects.

## 5.0 Conclusion

The landslide chronology developed in this study provides one of the most comprehensive reconstructions of Holocene slope instability in the Puget Lowland. Temporally, the results reveal broad clusters of deep-seated landslides that overlap the timing of known Holocene crustal earthquakes on the region's major fault zones. Two distinct peaks at ~1000 and ~1200 ybp coincide with the 1027 ybp Seattle Fault and 930–1290 ybp Tacoma Fault earthquakes, supporting the interpretation that both events contributed to an interval of heightened regional landslide activity.

https://doi.org/10.5194/egusphere-2025-6555
Preprint. Discussion started: 30 March 2026


Additional peaks near ~2000 ybp and ~3000 ybp align with the most recent ruptures on the Darrington–Devils Mountain and Southern Whidbey Island fault zones, respectively, indicating that multiple large earthquakes have influenced slope stability across the Holocene landscape. Although uncertainties in roughness-based ages preclude precise event-scale correlations, the temporal patterns are consistent with episodic, earthquake-driven mass-wasting pulses superimposed on a steady background rate of landsliding.

Landslide frequency-ratio-informed spatial analysis indicates that landslide density generally increases within 5-10 km of the studied fault traces, despite low overall susceptibility in those zones. This highlights a tectonic influence on the spatial distribution of landslides in the Puget Lowland. The clearest fault-proximal signals occur along the Seattle and Tacoma fault zones, where negative FR-distance slopes coincide with well-dated earthquake intervals. In contrast, elevated FR values around 20km from the DDMFZ likely reflect geomorphic and hydrologic controls within valley systems rather than direct coseismic triggering. These spatial trends, in combination with preservation-corrected frequency modeling, show that both earthquake forcing and intrinsic landscape susceptibility control where and when large landslides occur in the Puget Lowland.

Together, these findings demonstrate that Holocene crustal earthquakes have left detectable imprints in the landslide record, as evidenced by both temporal clustering and spatial concentration near active faults in the Puget Lowland. The regional extent of these signals implies that strong shaking during large crustal ruptures propagated broadly across the sediment-filled basin, triggering widespread landslides beyond the immediate fault zones. This work highlights the potential of roughness-calibrated landslide chronologies to serve as independent paleoseismic archives and the need to integrate geomorphic and seismologic evidence to refine future hazard assessment in tectonically active regions.

## Data availability

Landslide inventory data used in this study were obtained from the Washington Geological Survey statewide landslide inventory (WGS, 2020) and associated county-level mapping products for Pierce County, western King County, and portions of Snohomish County. All source inventories are publicly available through official WGS data repositories with these links:

https://doi.org/10.5194/egusphere-2025-6555
Preprint. Discussion started: 30 March 2026


https://dnr.wa.gov/washington-geological-survey/publications-and-data/geology-gis-data-and-databases, https://washingtonstategeology.wordpress.com/2017/07/20/pierce-county-landslide-inventory-released/, https://washingtonstategeology.wordpress.com/2019/01/24/new-landslide-inventory-of-western-king-county-published/, https://washingtonstategeology.wordpress.com/2022/07/28/new-landslide-inventory-of-portions-of-snohomish-county-published/. The complete subset of the analyzed inventory with the computed roughness and inferred ages is provided in the supplementary files. We have also provided a geospatial dataset containing the analyzed landslide polygons used in this study, including surface roughness values and inferred ages in a shapefile format. Matlab code for landslide history model was adopted from Herzig et al. (2024) and can be made available upon request. Python code for calculating surface roughness is available as the open-source pyTopoComplexity package (Lai et al., 2025).

## Authors contribution

AB (Adam Booth) and AD (Alison Duvall) originally proposed the study, acquired funding, and contributed to its conceptual development. OO (Obinna Ozioko) developed the methodology, compiled and refined the landslide inventory, conducted the surface roughness analysis, implemented and modified the landslide history modeling framework, performed all analyses, and led the writing of the manuscript. AB supervised the research throughout all stages, from study design through analysis and interpretation, and contributed to manuscript development and revision. AD contributed primarily to the interpretation of results and critical revision of the manuscript. EH (Erich Herzig) provided landslide history modeling code and technical guidance on its application and adaptation. All authors reviewed and approved the final manuscript.

## Competing interest

The authors declare that they have no competing interests.

## Acknowledgement

We acknowledge support from the National Science Foundation under Grant Nos. NSF 2000188 (AB) and 1953710 (AD), which funded this research. Additional fieldwork and sample analysis costs were supported by the Portland State University Department of Geology. We thank Emma

https://doi.org/10.5194/egusphere-2025-6555
Preprint. Discussion started: 30 March 2026


Rahalski and Nicholas Rudolph for their assistance with fieldwork. We are also grateful to Trevor Contreras for providing logistical support during fieldwork, including facilitating connections with local experts in the study area. We thank Ebele Esimai for her many hours of code review, discussion, and support throughout the research process. Grammarly was used as a writing assistant to improve grammar, readability, and clarity. The final content of this paper has been reviewed and edited by the authors.

## Financial support

This work was funded by the National Science Foundation (NSF) under Grant No. NSF 2000188 (AB) and 1953710 (AD).

## References

Allstadt, K. E., Jibson, R. W., Thompson, E. M., Massey, C. I., Wald, D. J., Godt, J. W., & Rengers, F. K. (2018). Improving near-real-time coseismic landslide models: Lessons learned from the 2016 Kaikōura, New Zealand, earthquake. *Bulletin of the Seismological Society of America*, *108*(3B), 1649-1664.

Atwater, B. F. (1999). Radiocarbon dating of a Seattle earthquake to AD 900–930, Seismol. Res. Lett. 70, no. 2, 232.

Ayalew, L., & Yamagishi, H. (2005). The application of GIS-based logistic regression for landslide susceptibility mapping in the Kakuda-Yahiko Mountains, Central Japan. *Geomorphology*, *65*(1-2), 15-31.

Badger, T. C. (2015), SR 530 MP 35 to 41 Geotechnical Study, Washington State Dep. of Transportation.

Black, B. A., J. K. Pearl, C. L. Pearson, P. T. Pringle, D. C. Frank, M. T. Page, B. M. Buckley, E. R. Cook, G. L. Harley, K. J. Heeter, et al. (2023). A multi-fault earthquake threat for the Seattle metropolitan region revealed by mass tree mortality, Sci. Adv. 9, no. 39, eadh4973, doi: 10.1126/sciadv.adh4973

https://doi.org/10.5194/egusphere-2025-6555
Preprint. Discussion started: 30 March 2026


Blakely, R. J., R. E. Wells, C. S. Weaver, and S. Y. Johnson (2002). Location, structure, and seismicity of the Seattle fault zone, Washington: Evidence from aeromagnetic anomalies, geologic mapping, and seismic-reflection data, Geol. Soc. Am. Bull. 114, 169–177.

Booth, A. M., S. R. LaHusen, A. R. Duvall, and D. R. Montgomery (2017). Holocene history of deep-seated landsliding in the North Fork Stillaguamish River valley from surface roughness analysis, radiocarbon dating, and numerical landscape evolution modeling, J. Geophys. Res. 122, no. 2, 456–472.

Booth, D. B., R. A. Haugerud, and K. Goetz Troost (2003), The Geology of Puget Lowland rivers, in Restoration of Puget Sound Rivers, edited by D. R. Montgomery et al., The Univ. of Washington Press, Seattle and London.

Bucknam, R. C., E. Hemphill-Haley, and E. B. Leopold (1992). Abrupt uplift within the past 1700 years at southern Puget Sound, Washington, Science 258, 1611–1614.

Chang, K. J., Taboada, A., & Chan, Y. C. (2005). Geological and morphological study of the Jiufengershan landslide triggered by the Chi-Chi Taiwan earthquake. Geomorphology, 71(3-4), 293-309.

Crozier, M. J. (2010). Deciphering the effect of climate change on landslide activity: A review. *Geomorphology*, *124*(3-4), 260-267.

Dadson, S. J., et al. (2004), Earthquake-triggered increase in sediment delivery from an active mountain belt, Geology, 32(8), 733–736, doi:10.1130/g20639.1.

Daniell, J. E., Schaefer, A. M., & Wenzel, F. (2017). Losses associated with secondary effects in earthquakes. Frontiers in Built Environment, 3, 30.

Dellow, S., Massey, C. I., McColl, S. T., Townsend, D. B., & Villeneuve, M. (2017). Landslides caused by the 14 November 2016 Kaikoura earthquake, South Island, New Zealand. In *Proceedings 20th NZGS Geotechnical Symposium*. New Zealand Geotechnical Society: Napier, New Zealand.

https://doi.org/10.5194/egusphere-2025-6555
Preprint. Discussion started: 30 March 2026


962 Esri, USGS, & NOAA. (2020). *World Hillshade [basemap]*. Esri. Retrieved from
963 https://www.arcgis.com/home/item.html?id=1b243539f4514b6ba35e7d995890db1d

964 Fan, X., G. Scaringi, O. Korup, A. J. West, C. J. van Westen, H. Tanyas, N. Hovius, T. C. Hales,
965 R. W. Jibson, K. E. Allstadt, et al. (2019). Earthquake-induced chains of geologic hazards:
966 Patterns, mechanisms, and impacts, Rev. Geophys. 57, no. 2, 421–503

967 Fan, X., Scaringi, G., Korup, O., West, A. J., van Westen, C. J., Tanyas, H., ... & Huang, R. (2019).
968 Earthquake-induced chains of geologic hazards: Patterns, mechanisms, and impacts. *Reviews of*
969 *geophysics*, *57*(2), 421-503.

970 Goetz, J. N., R. Bell, and A. Brenning (2014), Could surface roughness be a poor proxy for
971 landslide age? Results from the Swabian Alb, Germany, Earth Surf. Processes Landforms, 39,
972 1697–1704, doi:10.1002/esp.3630

973 Görüm, T., Tanyas, H., Karabacak, F., Yılmaz, A., Girgin, S., Allstadt, K. E., ... & Burgi, P. (2023).
974 Preliminary documentation of coseismic ground failure triggered by the February 6, 2023 Türkiye
975 earthquake sequence. *Engineering Geology*, *327*, 107315.

976 Haugerud, R. A. (2014), Preliminary interpretation of pre-2014 landslide deposits in the vicinity
977 of Oso, Washington, U.S. Geol. Surv. Open File Rep., 2014-1065.

978 Herzig, E., Duvall, A., Booth, A., Stone, I., Wirth, E., LaHusen, S., ... & Grant, A. (2024).
979 Evidence of Seattle Fault earthquakes from patterns in deep-seated landslides. *Bulletin of the*
980 *Seismological Society of America*, *114*(2), 1084-1102.

981 Hovius, N., P. Meunier, C.-W. Lin, H. Chen, Y.-G. Chen, S. Dadson, M.-J. Horng, and M. Lines
982 (2011), Prolonged seismically induced erosion and the mass balance of a large earthquake, Earth
983 Planet. Sci. Lett., 304(3–4), 347–355, doi:10.1016/j.epsl.2011.02.005.

984 Jacoby, G. C., P. L. Williams, and B. M. Buckley (1992). Tree ring correlation between prehistoric
985 landslides and abrupt tectonic events in Seattle, Washington, Science 258, no. 5088, 1621–1623.

986 Jibson, R. W. (1985). Landslides caused by the 1811-12 New Madrid earthquake, Doctoral
987 dissertation, Stanford University

https://doi.org/10.5194/egusphere-2025-6555
Preprint. Discussion started: 30 March 2026


Jibson, R. W., R. Grant, A. R., Witter, R. C., Allstadt, K. E., Thompson, E. M., & Bender, A. M. (2020). Ground failure from the Anchorage, Alaska, earthquake of 30 November 2018. *Seismological Research Letters*, *91*(1), 19-32.

Johnson, S. Y., S. V. Dadisman, J. R. Childs, and W. D. Stanley (1999). Active tectonics of the Seattle fault and central Puget Sound, Washington; Implications for earthquake hazards, Geol. Soc. Am. Bull. 111, 1042–1053

Kameda, J., Kamiya, H., Masumoto, H., Morisaki, T., Hiratsuka, T., & Inaoi, C. (2019). Fluidized landslides triggered by the liquefaction of subsurface volcanic deposits during the 2018 Iburi–Tobu earthquake, Hokkaido. *Scientific reports*, *9*(1), 13119.

Keefer, D. K. (1984). Landslides caused by earthquakes, Geol. Soc. Am. Bull. 95, no. 4, 406–421.

Keefer, D. K. (2000). Statistical analysis of an earthquake-induced landslide distribution—the 1989 Loma Prieta, California event. *Engineering geology*, *58*(3-4), 231-249.

Kelsey, H. M., Sherrod, B., Johnson, S. Y., & Dadisman, S. V. (2004). Land-level changes from a late Holocene earthquake in the northern Puget Lowland, Washington. *Geology*, *32*(6), 469-472.

Khazai, B., & Sitar, N. (2004). Evaluation of factors controlling earthquake-induced landslides caused by Chi-Chi earthquake and comparison with the Northridge and Loma Prieta events. Engineering geology, 71(1-2), 79-95.

LaHusen, S. R., A. R. Duvall, A. M. Booth, A. Grant, B. A. Mishkin, D. R. Montgomery, W. Struble, J. J. Roering, and J. Wartman (2020). Rainfall triggers more deep-seated landslides than Cascadia earthquakes in the Oregon Coast Range, USA, Sci. Adv. 6, no. 38, eaba6790, doi: 10.1126/sciadv.aba6790.

LaHusen, S. R., A. R. Duvall, A. M. Booth, and D. R. Montgomery (2016). Surface roughness dating of long-runout landslides near Oso, Washington (USA), reveals persistent postglacial hillslope instability, Geology 44, no. 2, 111–114

Lee, S., & Pradhan, B. (2007). Landslide hazard mapping at Selangor, Malaysia using frequency ratio and logistic regression models. *Landslides*, *4*(1), 33-41.

https://doi.org/10.5194/egusphere-2025-6555
Preprint. Discussion started: 30 March 2026


Lin, G.-W., H. Chen, N. Hovius, M.-J. Horng, S. Dadson, P. Meunier, and M. Lines (2008), Effects of earthquake and cyclone sequencing on landsliding and fluvial sediment transfer in a mountain catchment, Earth Surf. Processes Landforms, 33(9), 1354–1373, doi:10.1002/ esp.1716.

Luna, L. V., & Korup, O. (2022). Seasonal landslide activity lags annual precipitation pattern in the Pacific Northwest. *Geophysical Research Letters*, *49*(18), e2022GL098506.

Marc, O., Hovius, N., Meunier, P., Uchida, T., & Hayashi, S. (2015). Transient changes of landslide rates after earthquakes. Geology, 43(10), 883–886. https://doi.org/10.1130/G36961.1

McCalpin, J. (1984), Preliminary age classification of landslides for inventory mapping, Proc. 21st Engineering Geology and Soils Engineering Symposium, 99-120

McKean, J., & Roering, J. (2004). Objective landslide detection and surface morphology mapping using high-resolution airborne laser altimetry. *Geomorphology*, *57*(3-4), 331-351.

Méndez, J., Soto, G. J., Zamora, N., Vargas, A., Sjöbohm, L., Bonilla, E., ... & Baroň, I. (2009, August). Geología de los deslizamientos provocados por el Terremoto de Cinchona, Costa Rica (Mw 6, 2; 8 de enero del 2009) en la Ruta 126 (Varablanca-San Miguel). In *Presentado en el X Congreso Nacional de Geotecnia y V Encuentro Centroamericano de Geotecnistas. San José, Costa Rica*.

Meunier, P., N. Hovius, and J. A. Haines (2008). Topographic site effects and the location of earthquake induced landslides, Earth Planet. Sci. Lett. 275, nos. 3/4, 221–232.

Mickelson, K. A., Jacobacci, K. E., Contreras, T. A., Biel, A., & Slaughter, S. L. (2017). *Landslide inventory, susceptibility, and exposure analysis of Pierce County, Washington.* Washington Geological Survey Report of Investigations 39, 16 p. Includes 2 accompanying ESRI file geodatabases and 1 Microsoft Excel file.

Mickelson, K. A.; Contreras, T. A.; Allen, M. D.; Jacobacci, K. E.; Richard, E. M.; Gallin, W. N.; Fisher, Kara; Legoretta Paulín, Gabriel, 2022, Landslide inventory of portions of Snohomish County, Washington: Washington Geological Survey Report of Investigations 43, 7 p

https://doi.org/10.5194/egusphere-2025-6555
Preprint. Discussion started: 30 March 2026


Mickelson, K. A.; Jacobacci, K. E.; Contreras, T. A.; Gallin, W. N.; Slaughter, S. L., 2019, Landslide inventory of western King County, Washington: Washington Geological Survey Report of Investigations 41, 7 p. text, with an accompanying Esri file geodatabase

Miles, S. B., & Keefer, D. K. (2009). Evaluation of CAMEL—comprehensive areal model of earthquake-induced landslides. Engineering Geology, 104(1-2), 1-15.

Nelson, A. R., S. Y. Johnson, H. M. Kelsey, R. E. Wells, B. L. Sherrod, S. K. Pezzopane, L. A. Bradley, R. D. Koehler, and R. C. Bucknam (2003). Late Holocene earthquakes on the Toe Jam Hill fault, Seattle fault zone, Bainbridge Island, Washington, Geol. Soc. Am. Bull. 115, no. 11, 1388–1403.

Nelson, A.R., Personius, S.F., Buck, J., Bradley, L., Sherrod, B.L., Henley, G., II, Liberty, L.M., Kelsey, H.M., Witter, R.C., Koehler, R.D., III, and Schermer, E.R., 2008, Field and laboratory data from an earthquake history study of scarps in the hanging wall of the Tacoma fault, Mason and Pierce Counties, Washington: U.S. Geological Survey Scientific Investigations Map 3060, http:// pubs .er .usgs .gov /usgspubs /sim /sim3060

Oglesby, D. D., Archuleta, R. J., & Nielsen, S. B. (2000). The three-dimensional dynamics of dipping faults. *Bulletin of the Seismological Society of America*, *90*(3), 616-628.

Ozioko, O. H., & Igwe, O. (2020). GIS-based landslide susceptibility mapping using heuristic and bivariate statistical methods for Iva Valley and environs Southeast Nigeria. *Environmental monitoring and assessment*, *192*(2), 119.

Pánek, T. (2015). Recent progress in landslide dating: A global overview, Prog. Phys. Geogr. 39, no. 2, 168–198.

Perkins, J. P., M. E. Reid, and K. M. Schmidt (2017). Control of landslide volume and hazard by glacial stratigraphic architecture, northwest Washington State, USA, Geology 45, no. 12, 1139–1142.

Personius, S. F., R. W. Briggs, A. R. Nelson, E. R. Schermer, J. Z. Maharrey, B. L. Sherrod, S. A. Spaulding, and L. A. Bradley (2014), Holocene earthquakes and right-lateral slip on the left-lateral

https://doi.org/10.5194/egusphere-2025-6555
Preprint. Discussion started: 30 March 2026


Darrington-Devils Mountain fault zone, northern Puget Sound, Washington, Geosphere, 10(6), 1482–1500, doi:10.1130/ges01067.1.

Porter, S. C., and T. W. Swanson (1998), Radiocarbon age constraints on rates of advance and retreat of the Puget lobe of the Cordilleran ice sheet during the last glaciation, Quat. Res., 50(3), 205–213, doi:10.1006/qres.1998.2004.

Ramsey, C. B. (2009). Bayesian analysis of radiocarbon dates. *Radiocarbon*, *51*(1), 337-360.

Reimer, P. J., Austin, W. E., Bard, E., Bayliss, A., Blackwell, P. G., Ramsey, C. B., ... & Talamo, S. (2020). The IntCal20 Northern Hemisphere radiocarbon age calibration curve (0–55 cal kBP). *Radiocarbon*, *62*(4), 725-757.

Schuster, R. L., NietoThomas, A. S., O'Rourke, T. D., Crespo, E., & Plaza-Nieto, G. (1996). Mass wasting triggered by the 5 March 1987 Ecuador earthquakes. Engineering geology, 42(1), 1-23.

Serey, A., L. Piñero-Feliciangeli, S. A. Sepúlveda, F. Poblete, D. N. Petley, and W. Murphy (2019). Landslides induced by the 2010 Chile megathrust earthquake: A comprehensive inventory and correlations with geological and seismic factors, Landslides 16, 1153–1165

Sherrod, B. L. (2001). Evidence for earthquake-induced subsidence about 1100 yr ago in coastal marshes of southern Puget Sound, Washington, GSA Bull. 113, no. 10, 1299–1311.

Sherrod, B. L., R. C. Bucknam, and E. B. Leopold (2000). Holocene relative sea level changes along the Seattle fault at restoration point, Washington, Quat. Res. 54, no. 3, 384–93

Sherrod, B. L., R. J. Blakely, C. S. Weaver, H. M. Kelsey, E. Barnett, L. Liberty, K. L. Meagher, and K. Pape (2008). Finding concealed active faults: Extending the southern Whidbey Island fault across the Puget Lowland, Washington, J. Geophys. Res. 113, no. B5, doi: 10.1029/2007JB005060.

Sherrod, B. L., T. M. Brocher, C. S. Weaver, R. C. Bucknam, R. J. Blakely, H. M. Kelsey, A. R. Nelson, and R. Haugerud (2004). Holocene fault scarps near Tacoma, Washington, USA. Geology 32, no. 1, 9–12.

https://doi.org/10.5194/egusphere-2025-6555
Preprint. Discussion started: 30 March 2026


Slaughter, S. L.; Burns, W. J.; Mickelson, K. A.; Jacobacci, K. E.; Biel, Alyssa; Contreras, T. A., 2017, Protocol for landslide inventory mapping from lidar data in Washington State: Washington Geological Survey Bulletin 82, 27 p. text, with 2 accompanying ESRI file geodatabases and 1 Microsoft Excel file.

Struble, W. T., Roering, J. J., Burns, W. J., Calhoun, N. C., Wetherell, L. R., & Black, B. A. (2021). The preservation of climate-driven landslide dams in western Oregon. *Journal of Geophysical Research: Earth Surface*, *126*(4), e2020JF005908.

Styron, R. H., & Sherrod, B. (2021). Improving paleoseismic earthquake magnitude estimates with rupture length information: Application to the Puget Lowland, Washington State, USA. *Bulletin of the Seismological Society of America*, *111*(2), 1139-1153.

Tanyaş H, van Westen CJ, Allstadt KE, et al (2017) Presentation and analysis of a worldwide database of earthquake-induced landslide inventories. J Geophys Res Earth Surf 122https://doi.org/10.1002/ 2017JF004236

Tanyaş, H., Görüm, T., Fadel, I., Yıldırım, C., & Lombardo, L. (2022). An open dataset for landslides triggered by the 2016 Mw 7.8 Kaikōura earthquake, New Zealand. *Landslides*, *19*(6), 1405-1420.

Troost, K. G., & Booth, D. B. (2008). Geology of Seattle and the Seattle area, Washington.

Tubbs, D. W. (1974), Landslides in Seattle, Information Circular 52, State of Washington, Dept. of Natural Resources, Olympia, Washington.

U.S. Geological Survey (USGS). (2022a). *Scenario ShakeMap: M 7.2 Seattle Fault Zone earthquake (wa22sfz01_se).* U.S. Geological Survey Earthquake Hazards Program. Retrieved [Month Year], from https://earthquake.usgs.gov/scenarios/eventpage/wa22sfz01_se/shakemap

U.S. Geological Survey (USGS)**.** (2022b). *Scenario ShakeMap: M 7.1 Tacoma Fault Zone earthquake (wa22tf01_se).* U.S. Geological Survey Earthquake Hazards Program. Retrieved [Month Year], from https://earthquake.usgs.gov/scenarios/eventpage/wa22tf01_se/shakemap

https://doi.org/10.5194/egusphere-2025-6555
Preprint. Discussion started: 30 March 2026


**U.S. Geological S**urvey (USGS). (2022c). *Scenario ShakeMap: M 7.2 Southern Whidbey Island Fault Zone earthquake (wa22swif01_se).* U.S. Geological Survey Earthquake Hazards Program. Retrieved from https://earthquake.usgs.gov/scenarios/eventpage/wa22swif01_se/shakemap

Underwood, A., Adam, M. B., LaHusen, S., Herzig, E., Duvall, A., Malick, G., ... & Streig, A. (2025). Most recent surface rupturing earthquake on the Boulder Creek Fault triggered bedrock landslides in the Nooksack watershed, Whatcom County, Washington. *Geomorphology*, 109912.

Walsh, T.J., Polenz, M., Logan, R.L., Lanphere, M.A., and Sisson, T.W., 2003, Pleistocene tephrostratigraphy and paleogeography of the southern Puget Sound near Olympia, Washington, in Swanson, T.W., ed., Western Cordillera and Adjacent Areas: Geological Society of America Field Guide 4, p. 225–236, doi:10.1130/0-8137-0004-3.225

Wartman, J., L. Dunham, B. Tiwari, and D. Pradel (2013). Landslides in eastern Honshu induced by the 2011 Tohoku earthquake, Bull. Seismol. Soc. Am. 103, no. 2B, 1503–1521, doi: 10.1785/ 0120120128.

Washington Geological Survey (2020). Landslide protocol inventory mapping—GIS data, February, 2020: Washington Geological Survey Digital Data Series 19, version 2.0, previously released January 2019, available at https://fortress.wa.gov/dnr/ geologydata/publications/data_download/ ger_portal_landslide_database.zip (last accessed June 2020)

Washington Geological Survey (WGS). (2021). *M 7.4 Scenario Earthquake—Darrington–Devils Mountain Fault Zone (western segment).* Washington Geological Survey Report 25-09. https://www.dnr.wa.gov/Publications/ger_seismic_scenario_devils_mt_west.pdf

Xu, C. (2015). Preparation of earthquake-triggered landslide inventory maps using remote sensing and GIS technologies: Principles and case studies. *Geoscience Frontiers*, *6*(6), 825-836.

Xu, C., Xu, X. W., Yao, X., & Dai, F. C. (2014). Three (nearly) complete inventories of landslides triggered by the Wenchuan Mw 7.9 earthquake of 12 May 2008. *Landslides*, 11(3), 441–461. https://doi.org/10.1007/s10346-013-0404-6

https://doi.org/10.5194/egusphere-2025-6555
Preprint. Discussion started: 30 March 2026


Xu, C., Xu, X., Shyu, J. B. H., Gao, M., Tan, X., Ran, Y., & Zheng, W. (2015). Landslides triggered by the 20 April 2013 Lushan, China, Mw 6.6 earthquake from field investigations and preliminary analyses. *Landslides*, *12*(2), 365-385.

Xu, Y., Liu-Zeng, J., Allen, M. B., Du, P., Zhang, W., Li, W., & Tian, Q. (2022). Understanding historical earthquakes by mapping coseismic landslides in the Loess Plateau, northwest China. *Earth Surface Processes and Landforms*, *47*(9), 2266-2282.

Yanites, B. J., Clark, M. K., Roering, J. J., West, A. J., Zekkos, D., Baldwin, J. W., ... & Pierce, J. (2025). Cascading land surface hazards as a nexus in the Earth system. *Science*, *388*(6754), eadp9559.

Yount, J. C., J. P. Minard, and G. R. Dembroff (1993). Geologic Map of Surficial Deposits in the Seattle 30′ × 60′ quadrangle, Open-File Rept. 93-233, U.S. Geological Survey, Washington, D.C.

Zheng, X., Han, L., He, G., Wang, N., Wang, G., & Feng, L. (2023). Semantic segmentation model for wide-area coseismic landslide extraction based on embedded multichannel spectral–topographic feature fusion: A case study of the Jiuzhaigou Ms7. 0 earthquake in Sichuan, China. *Remote Sensing*, *15*(4), 1084.